Politecnico di Torino

Department of Environment, Land and Infrastructure Engineering

Master of Science in Georesources and Geoenergy Engineering

Sealing properties of the cap rock for underground gas storage safety

Supervisors

Prof. Vera Rocca

Dr. Nacer Benlalam

Candidate

Leonardo Arana Parodi

This page intentionally left blank.

Abstract

Climate change mitigation requires a multifaced approach and one of the most promising technologies is subsurface fluid storage in porous media. However, this technology is not exempt of risks. The leakage of fluid stored through the cap rock is a critical concern and, in consequence, a key parameter to determine in these operations is the capillary sealing efficiency of the cap rock standardly determined by long and expensive laboratory experiments of fluid flow through tight or ultra-tight core samples.

This thesis investigates the influence of different conditions (i.e. core sample length and temperature) in the breakthrough pressure obtained from the standard (step-by-step) test in laboratory. A multidisciplinary approach was implemented combining routine core analysis to characterize the core samples (e.g. porosity, and absolute permeability) with step-by-step laboratory tests and numerical simulations in COMSOL Multiphysics® to obtain a full understanding of the phenomenon from a theoretical and experimental views. The results from the simulations showed good agreement with the experimental data, showing their potential to optimize the experiments and giving an alternative approach to support the capillary breakthrough pressure laboratory evaluation.

The work includes:

- **Core sample characterization**: Analysis and description of the core samples using data available in the literature (e.g. pore size distribution, and mineralogy) and routine core analysis performed on different samples (e.g. porosity, and absolute permeability).

- **Step-by-step tests:** Perform of step-by-step tests to obtain the breakthrough pressure under different conditions.

- **Numerical simulations:** Simulations of the phenomenon through simplified capillary bundle models using COMSOL Multiphysics® focusing on the hydrodynamic phenomenon to obtain the breakthrough pressure.

- **Comparative analysis, results and discussion:** Comparison and analysis of the results between the different conditions of the experiments performed and with the simulations done showing that there is an influence of the absolute permeability and length over the breakthrough pressure while no relationship was found between the temperature and the breakthrough pressure.

Contents

List of Figures

List of tables

1. Introduction

The Paris Agreement signed by 198 countries and ratified, up to October of 2024, by 195 countries set an ambitious but necessary goal for the future of the world. According to its article 2 (a), the objective of this agreement is to " Holding the increase in the global average temperature to well below 2°C above pre-industrial levels and pursuing efforts to limit the temperature increase to 1.5°C above pre-industrial levels, recognizing that this would significantly reduce the risks and impacts of climate change" [1].

The International Energy Agency established in the World Energy Outlook 2023 3 main scenarios for the future of the energy industry: the Net Zero Emissions by 2050 (NZE) Scenario which is the optimistic one and coincides with the goal of the Paris Agreement, the Announced Pledge Scenario (APS) which is based on the commitments announced by the governments of the different countries in the world which is considered the most likely scenario and the Stated Policies Scenario (STEPS) which is considered the conservative scenario [2].

As seen in Figure 1, even in the pessimistic scenario, the peak of the production of fossil fuels (Coal, Oil and Natural Gas) is reached before 2030.

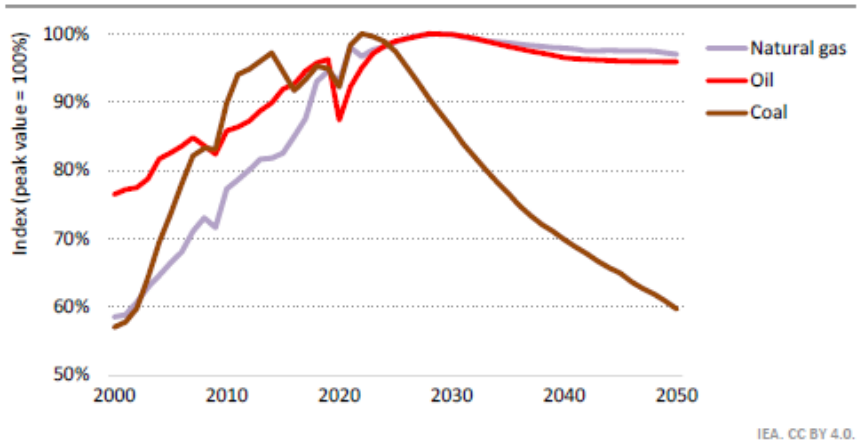

Figure 1: Forecast of fossil fuels production - WEO (STEPS) [2]

These changes can only be supported by the increasing of investment in renewable energies (i.e. clean energies) as we can see in Figure 2:

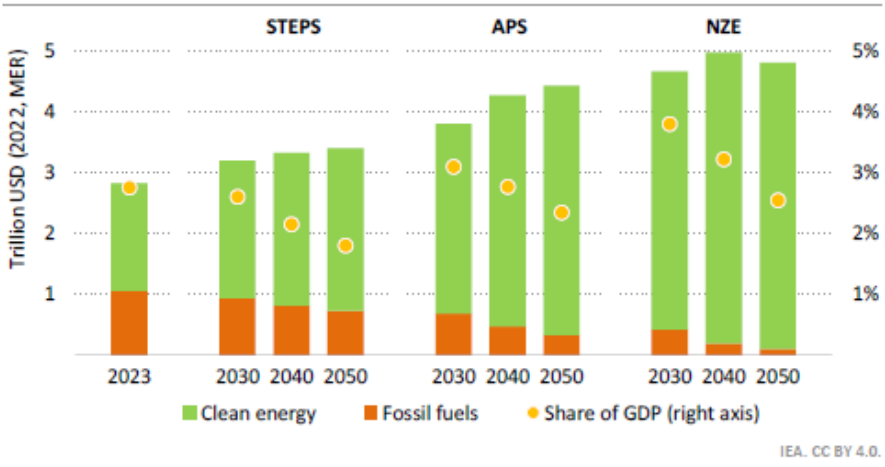

Figure 2: Investment projected in the different types of energies. [2]

The decarbonization process is being faced in several ways by the industry, as we can see in Figure 3.

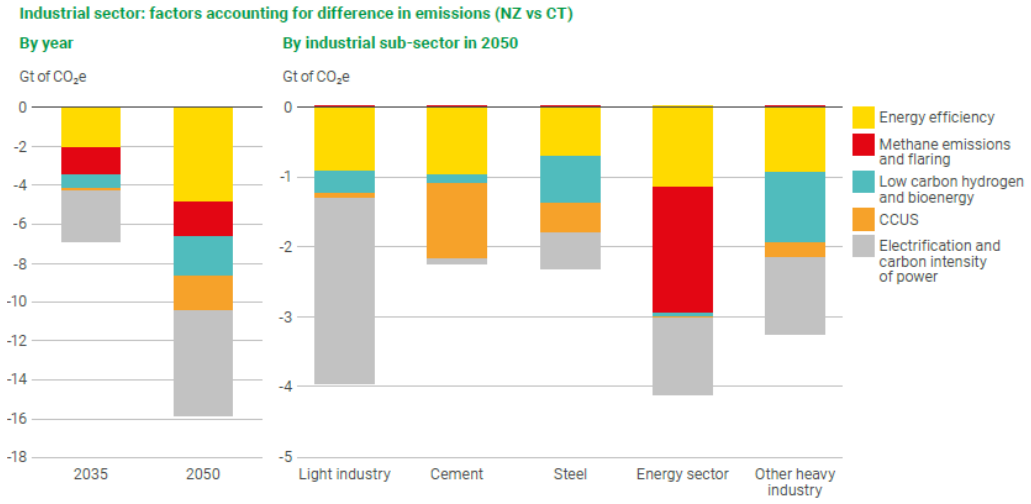

Figure 3: Factors accounting for difference in emissions. BP Energy Outlook. [3]

The processes of Underground Fluid Storage can be divided in temporal energy storage and final disposal of residual products of combustion.

Temporal Energy Storage

This option includes the storage of hydrocarbons, usually methane (UGS), or hydrogen (UHS) for a certain period to be withdraw and used when needed. The typical scheme used in the energy industry is to store methane in summer (when there is an excess of production over demand) and withdraw them in winter (when the production cannot satisfy demand).

Final Disposal of Residual products of combustion

In this case the aim is to store the residual products of combustion: Carbon dioxide and ensure no leakage. It is usually called Carbon Capture and Storage (CCS) or Carbon Capture Utilization and Storage (CCUS) if there is an option of utilizing the CO_2 for other products before the final storage. The storage of carbon dioxide is also called Carbon Sequestration.

Both options contribute in one way (energy transition to clean energies in the first case) or another (reduction of carbon dioxide in the atmosphere in the second case) to the decarbonization process.

In the case of energy transition to clean energies, UGS has played an important role in supporting energy security and seasonal supply balancing, particularly in some European countries since the second half of the 20th century (e.g. Minerbio in Italy and Bergermeer in The Netherlands). In contrast, UHS is an emerging technology still under development with a great potential in the future but with no ongoing projects.

On the other hand, CO2 injection has been used for decades in the oil and gas industry as an Enhanced Oil Recovery technique. The first large scale CO_2-EOR project was implemented in 1972 in the SACROC and North Cross Fields in Texas, U.S.A. However, CCS is a more recent development that started getting importance in the 21st century and with just a few projects in operation like Sleipner in Norway and Boundary Dam in Canada among others.

In Figure 4 the potential of this Underground Fluid Storage is compared with other options existing in the market.

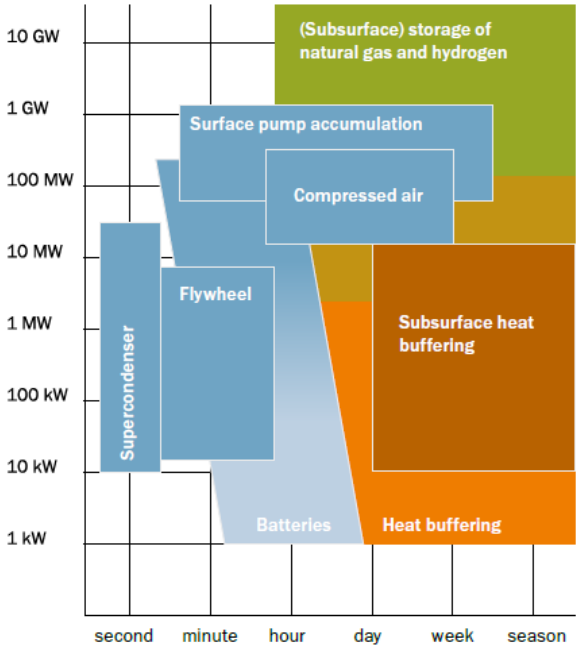

Figure 4: Relative Capacity and duration of some technologies to store energy. [4]

The International Energy Agency estimates the current carbon capture utilization and storage (CCUS) capacity in 50 million tons (Mt) of CO_2 per year and projects a capacity of 435 Mt of CO_2 in 2030 with a gap of 589 to reach the Net Zero Scenario [5].

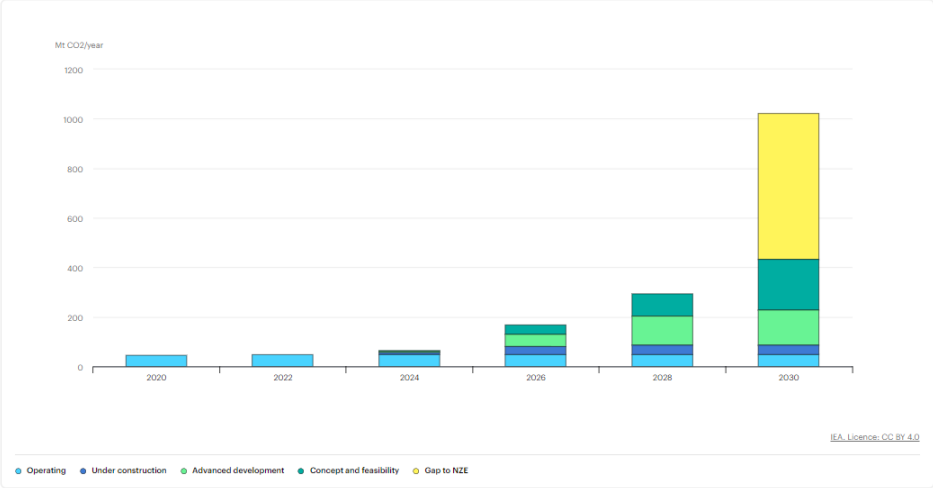

Figure 5: IEA (2023), Capacity of current and planned large-scale CO2 capture projects vs. the Net Zero Scenario, 2020-2030, IEA [5]

According to Cedigaz [6], in 2022, the facilities for gas storage were distributed by region in the following way.

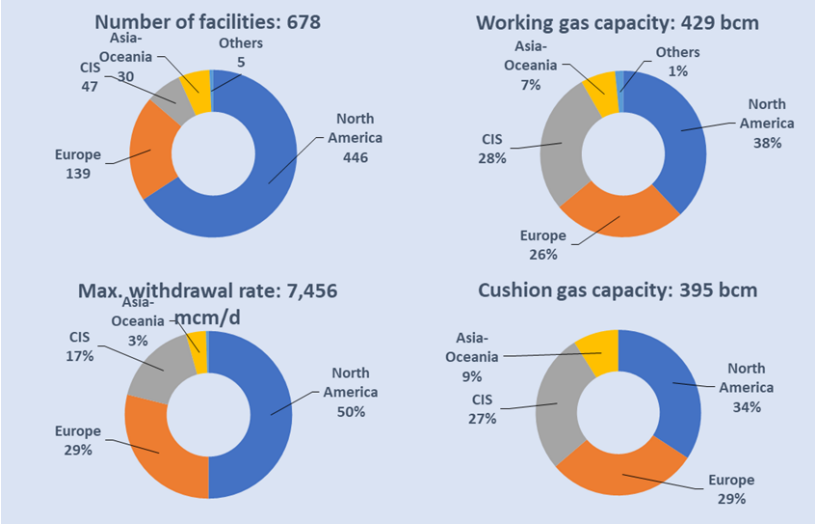

Figure 6: Global Underground Gas Storage distribution in 2022. Cedigaz [6].

As seen previously, Underground Fluid Storage is a fundamental technology for the industry, but it is not exempt of risks. According to the literature, these are the main technical risks that this type of project can face:

- Induced seismicity
- Elevation movements of the surface (Subsidence or Uplift)
- Leakage:
    - Through the cap rock (Overestimation of seal capacity)
    - Along fractures or across faults previously considered sealing
    - Injected fluids spilling out of the reservoir

One issue that has taken particularly attention of stakeholders and citizens is the induced seismicity. Some examples of this problem were observed in:

Castor Project, Spain

Seismic activity was detected together with a test of the fill up part of the project of gas storage in an oil depleted reservoir with peaks of Maximal moment magnitude M_w 4.3 earthquake and these events were correlated with the injection activity performed [7].

Cogdell, U.S.A.

The injection activity of this oil field started in 2001, but the volumes are almost constant since 2004. In 2006 some seismic events were reported by the National Earthquake Information Center (NEIC) after a period of seismic silence (1983 – 2005) according to the same entity. The worst event was one detected on September 11th, 2011, of M_w 4.4 [8].

One of the risks that has a direct impact on the common live of the population near the fields are the elevation movements.

Groningen, Netherlands

The Groningen gas field is a good example of surface elevation changes due to subsurface activities. In this case, a subsidence up to 37cm was observed due to gas production [9].

A fundamental characteristic of the reservoir is to contain the fluid injected in a safety way. The leakage paths may include wells (lack of well or cement integrity), Cap rock and/or faults.

In Salah, Algeria

Injection in this project started in 2004. And, after 3.8 Mt of CO_2 injected, the possibility of a vertical leakage into the caprock was detected in 2010 thanks to the monitoring techniques used (seismic and geomechanics data). The operator took the decision of reducing the rate of injection in June 2010 and suspend the injection in June 2011 [10].

The cap rock plays a key role to ensure the storage of fluids in a safety way for the time that it is required (cycles of one year in the case of UHS or UGS and in the long time in the case of CCS) and, consequently, a correct characterization of it is fundamental for any project. The main characteristics to determine from a cap rock are capillary sealing efficiency, heterogeneities [11], mechanical integrity [11] and potential geochemical interactions between the fluids injected and the minerals in the cap rock.

One of the main characteristics of the cap rock is the capillary sealing efficiency which depends mainly on the properties of the fluids, the rock and the interactions between both. Among the factors that influence it, one can found:

Type	Variable
Characteristics of the Cap rock	Permeability Pore throat size Heterogeneity Height Mineral composition
Characteristics of the fluids	State of the fluid injected (gas, liquid or supercritical) Interfacial tension between the fluid injected and the brine present in the cap rock Salinity of the brine present in the cap rock Densities of the fluid implicated
Fluids – rock interactions	Contact angle (wettability)

Table 1: Factors that influence the capillary sealing efficiency.

1.1. Scope of study

This thesis investigates the influence of different conditions (i.e. core sample length and temperature) in the breakthrough pressure obtained from the standard (step-by-step) test in laboratory. A multidisciplinary approach was implemented combining routine core analysis to characterize the core samples (e.g. porosity, and absolute permeability) with step-by-step laboratory tests and numerical simulations in COMSOL Multiphysics® to obtain a full understanding of the phenomenon from a theoretical and experimental views.

The tests were performed on the Scioto sandstone (U.S.A.). This rock is part of the Mississippian formation, and it is commonly used to perform research in subsurface porous media. Even if it is not a real cap rock formation, it was selected for its availability on market as a standard, so it represents a well determined domain for the investigation developed in the present work.

The work includes:

- **Core sample characterization**: Analysis and description of the core samples using data available in the literature (e.g. pore size distribution, and mineralogy) and routine core analysis performed on different samples (e.g. porosity, and absolute permeability).

- **Step-by-step tests:** Perform of step-by-step tests to obtain the breakthrough pressure under different conditions.

- **Numerical simulations:** Simulations of the phenomenon through simplified capillary bundle models using COMSOL Multiphysics® focusing on the hydrodynamic phenomenon to obtain the breakthrough pressure.

- **Comparative analysis, results and discussion:** Comparison and analysis of the results between the different conditions of the experiments done and with the simulations performed.

2. The underground storage of gases and cap rock sealing efficiency

The underground fluid storage options can be classified based on their geological location. These include saline aquifers, depleted oil and gas reservoirs, and salt caverns for the storage of methane, hydrogen, and carbon dioxide, as well as coal seams, basalts, abandoned mines, and hydrocarbon-rich shales, for carbon dioxide storage. In this study, we focus on depleted oil and gas reservoirs and saline aquifers.

Depleted reservoirs offer several advantages: they typically provide a larger storage capacity compared to batteries, there is usually extensive knowledge of the petrophysical and mechanical properties of the reservoir rock, the storage volume can be estimated with high accuracy, existing surface facilities from the production phase are often still available and the reservoir pressure is generally lower than the original due to prior depletion. On the other hand, the main advantage of saline aquifers over oil and gas reservoirs is their typically larger areal extent, which can result in greater overall storage capacity.

The geological storage options involve several trapping mechanisms, which can be classified as physical or geochemical:

Type of mechanisms	Mechanisms	Physical explanation
Physical trapping	Structural trapping	The fluid injected cannot migrate due to the presence of a low-permeability cap rock.
	Stratigraphic trapping	The fluid injected cannot migrate due to variations in the petrophysical properties of the rock.
	Hydrodynamic trapping	Occurs when there is no closed trap, allowing injected fluids to migrate horizontally over long distances.
	Residual trapping	The carbon dioxide becomes disconnected into an immobile fraction due to a first displacement of water by carbon dioxide followed by an imbibition process in the reservoir rock.
Geochemical trapping	Solution trapping	Carbon dioxide dissolves in water to form carbonic acid H_2CO_3.
	Ionic trapping	Follows solution trapping and involves the release of hydrogen ions H^+, forming bicarbonate HCO_3^-, and potentially carbonate ions CO_3^{2-} after another liberation of ions H^+.
	Mineral trapping	Involves geochemical reactions between carbonate ions CO_3^{2-} and minerals present in the rock.

Table 2: Trapping mechanisms

The main elements of the underground storage in oil/gas reservoirs and aquifers system are the Reservoir rock and the Cap rock.

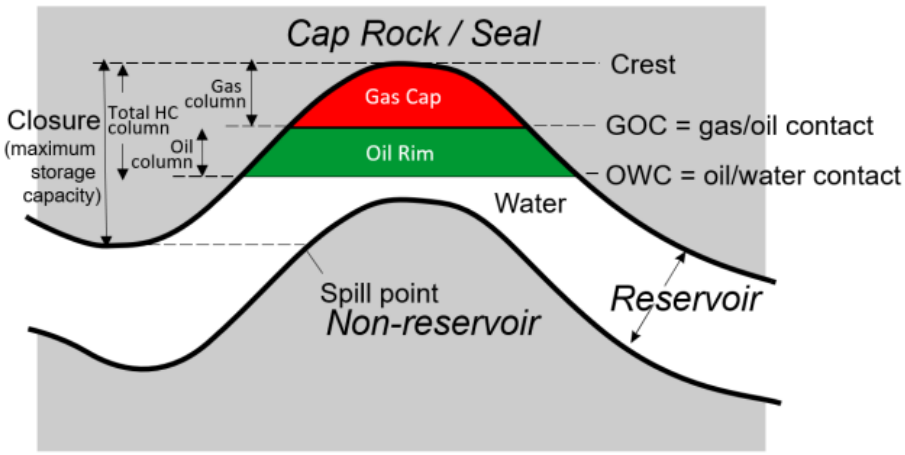

Figure 7: Petroleum trap elements. [12]

The reservoir rock is the formation where the fluid is injected. For this purpose, properties like storage capacity and injectivity are fundamental.

The storage capacity accounts for the volume of fluid that the reservoir rock can store. This value depends, mainly, on the structure of the reservoir (area and height), porosity and residual water saturation of the reservoir.

The injectivity on the other hand, determine the flow rate of fluid that a well can inject per unit of time and depends, mainly, on the permeability of the formation, difference of pressure between the reservoir and the bottom hole of the well and properties of the fluid like viscosity and density

Conventional reservoir rocks are divided in sandstones and carbonates. Sandstones are sandy sediments that suffered from natural compaction and cementation. These rocks have more than 50% of terrigenous siliciclastic grains. With porosities that, usually, ranges from 5 – 30% (porosities lower than 5% are usually not interesting from a commercial point of view for the energy industry and porosities above 35% are unusual) and permeabilities from 10 mD to more than 1000 mD (permeabilities lower than 10 mD are considered “tight” reservoirs and needs some special techniques for production like hydraulic fracturing), they constitute about the 60% of all the reservoirs in the world and are made, mainly, of 3 constituents that can be classified in 2 types according to where they were formed [13]:

- Allogenic minerals: Formed elsewhere and transported into the area of deposition (i.e. Grains and Matrix).
- Authigenic minerals: Formed at the site of deposition, either by direct chemical precipitation or by later diagenetic processes (i.e. Cement).

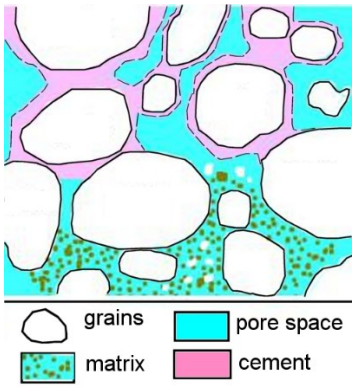

Figure 8: Constituents of sandstones [14]

The grains of sandstones are composed of quartz, feldspars, micas and minerals. The size ranges from 0.0625 mm to 2 mm, but they can also contain some amounts of different size grains. We can classify the components of the grains using the following structure [15]:

Type	Components	Examples
Major minerals	Quartz	Monocrystalline, polycrystalline, etc
	Feldspars	Alkali, plagioclase, etc.
	Fine micas	Muscovite, biotite
	Clay minerals	Kaolinite, Illite, etc.
Accessory minerals	Coarse micas	Muscovite, biotite
	Heavy minerals	Zircon, tourmaline, etc.
Rock fragments	Igneous rock fragments	Volcanic rocks
	Metamorphic rock fragments	Metaquartzite, phyllite, etc.
	Sedimentary rock fragments	Sandstone, siltstone, etc.
Chemical cements	Silicate minerals	Micro quartz, opal, etc.
	Carbonate minerals	Calcite, aragonite, etc.
	Iron oxide minerals	Hematite, limonite, etc.
	Sulphate minerals	Anhydrite, barite, etc.

Table 3: Classification of components in sandstones

The matrix is a very fine size material (<0.03 mm) present within interstitial pore space among the framework grains. The matrix is usually composed by clay minerals (most common), fine-size micas, quartz and Feldspars. [15]. Cementing materials can be silicate minerals like quartz and opal or non-silicate minerals like calcite and dolomite. All cementing materials are secondary minerals that form in sandstones after deposition and during burial [15].

Carbonate rocks are chemical/biochemical sedimentary rocks primary composed (more than 50%) by carbonate minerals. Due to its chemical/biochemical characteristics, they develop a secondary porosity during diagenesis (due to dissolution or fracturing of carbonate grains) that, in some cases, enhance the primary porosity and permeability. Can be divided based on the mineralogy into limestones and dolomites (dolostones).

Limestones are rocks composed, mainly of calcium carbonate ($CaCO_3$) as calcite or aragonite [15]. There are several ways to classify Limestones. Two of the most used in the energy industry are

Folk Classification (distinguish 3 basic components: sediment grains, microcrystalline lime mud and sparry calcite cement) and Dunham Classification (based on the nature of the framework) [16].

Dolostones are rocks composed mainly of mineral dolomite ($CaMg(CO_3)_2$). Dolomite is in most cases not formed directly, but as a secondary mineral because of reactions between different forms of $CaCO_3$ and Mg^{2+} [16]:

$$2CaCO_3 + Mg^{2+} = CaMg(CO_3)_2 + Ca^{2+} \qquad \textit{Equation 1}$$

2.1. The cap rock sealing efficiency

The cap rock (also called seal rock) is the formation that prevents the migration of fluids out of the reservoir. Properties like permeability, thickness and fracture pressure are fundamental for this purpose as well as the sealing efficiency. The most common types of cap rocks are Silicates Mudrocks (i.e. Siltstones, Mudstones and Shales), Cemented Carbonates and Evaporites.

- **Mudrocks**

  Mudrocks are rocks composed mainly (more than 50%) of terrigenous siliciclastic grains (quartz, feldspars, micas and minerals). The difference with sandstones is the size of most of the grains, as we can see in the following table taken from the Udden-Wentworth classification:

Consolidated rock	Name	Size range (mm)
Siltstone	Coarse silt	0.031 – 0.0625
	Medium silt	0.0156 – 0.031
	Fine silt	0.0078 – 0.0156
	Very fine silt	0.0039 – 0.0078
Mudstone and Shale	Clay	0.00006 – 0.0039

Table 4: Udden-Wentworth grain size scale for siltstones, mudstones and shales

As seen in Table 4, most grain sizes of siltstones range from 0.0039 to 0.0625 mm, but they may also contain some percentages of clay size grains. This influences in the porosity and the permeability of these rocks and makes them suitable (but not ideal) cap rocks. Usually, this type of cap rocks can trap few tens of meters of hydrocarbons.

Mudstones and shales are composed of clay size grains (<0.0039 mm) (Table 4). Because of this, both types of rocks are ideal cap rocks due to their low permeability and high seal capacity. The main difference between both is the fissility (lamination) in the structure of shales.

Both types of rocks are mainly composed by [16] [17]:

Type	Components
Silicate minerals	Quartz
	Feldspars
	Zeolites
Clay minerals	Kaolinite
	Illite
	Smectite
	Muscovite
	Chlorite
Oxides and hydroxides	Hematite
	Goethite
	Limonite
	Gibbsite
Carbonate minerals	Calcite
	Dolomite
	Siderite
Sulphur minerals	Gypsum
	Anhydrite
	Barite
	Pyrite

Table 5: Main components in mudstones and shales

- **Carbonates**

  As seen in section 2, there are 2 types of carbonates according to the composition (Limestones and Dolostones). The main difference between the carbonates as reservoir and cap rocks is the type of support of the rock. Reservoir rocks are grain-supported while cap rocks are cemented carbonates. The great disadvantage of carbonates as cap rocks is their chemical instability and risk of reaction with carbon dioxide. Due to its composition, Dolostones are less soluble than Limestones which can make them effective seals. Cemented carbonates are mainly composed by Calcium carbonate, Dolomite, Quartz, Illite, Kaolinite and Smectite.

- **Evaporites**

  Evaporites are sedimentary rocks formed by the evaporation of saline water. Evaporites contain several salt minerals which are too soluble to be precipitated in normal marine or continental environments. The most important are Chlorides, Sulphates, Alkaline carbonates and Ca-Mg carbonates.

  The result of the process of evaporation depends on the evaporation rate and the exchange of fresh water with sources outside of the basin. If the rate of evaporation is lower than the rate of supply of fresh water, the result is going to be a freshwater basin. If the rate of evaporation is higher than the rate of supply of fresh water but there is still a rate of fresh water, there is going to develop a high salinity sea. In the last case, if there is no supply of fresh water (due to a physical barrier), the result is going to be an evaporite [16].

The main petrophysical parameters to consider in the cap rocks are porosity and permeability.

Porosity is the capacity of a rock to contain fluids. We can classify this property in total porosity (i.e. pore volume of a rock divided the total volume of the rock) and effective porosity (i.e. interconnected volume of the rock divided by the total volume of the rock).

According to Glover [18], porosity is governed by grain size, grain packing, grain shape, grain size distribution and changes during sedimentation (i.e. compaction, fracturing, deformation, dissolution, precipitation and mineralogical changes). Porosity can be measured in the laboratory with disaggregation of the rock sample (i.e. total porosity) and imbibition, mercury injection or gas expansion (i.e. effective porosity).

On the other hand, absolute permeability is the capacity of the rock to allow the flow of fluids in one direction. Taking this into account, the absolute permeability is not a scalar but a vector. According to Glover [18] and Tiab and Donaldson [19], the absolute permeability is controlled by porosity, bedding (i.e. lamination), pore geometry, diagenetic processes and stress conditions. The absolute permeability can be measured in the laboratory with steady state methods or unsteady state methods.

The physical phenomena that control the sealing efficiency depends both on the viscous and capillary forces. While the first is explained by the Darcy law (Equation 2), the second one uses the Young – Laplace equation (Equation 6).

$$v = \frac{q}{A} = -\frac{k}{\mu}(\nabla p - g\rho\nabla z) \qquad \textit{Equation 2}$$

Where:

v: $velocity$

q: $rate$

A: $cross\ sectional\ area$

k: $permeability$

μ: $viscosity$

∇p: $pressure\ gradient$

g: $gravitational\ constant$

ρ: $density$

∇z: $gradient\ in\ the\ elevation\ head$

If the fluids injected in the reservoir rock are lighter than the formation brine, like in UHS, UGS and CCS, they tend to go upward, penetrate the cap rock and migrate out from the reservoir due to the buoyant force. The fluids injected in the reservoir rock less dense than water (oil and any kind of gas) trapped in a reservoir under hydrostatic conditions, represents an equilibrium state between buoyant forces trying to move the fluids upward and the capillary pressures in the cap rock that resist that movement. The buoyancy pressure is described with the following equation [20]:

$$P_b = \frac{F_b}{A} = h_{fl} g (\rho_w - \rho_{fl})$$ *Equation 3*

Where:

P_b: $Buoyancy\ pressure$

F_b: $Buoyancy\ force$

A: $Area$

h_{fl}: $Height\ of\ column\ of\ the\ fluid\ less\ dense\ than\ water$

g: $Gravity\ acceleration$

ρ_w: $Density\ of\ water$

ρ_{fl}: $Density\ of\ the\ fluid\ less\ dense\ than\ water$

Figure 9 illustrates the way the capillary pressure acts as a barrier to prevent fluid leakage in the cap rock. If the pressure of the non-wetting fluid (methane, nitrogen or hydrogen) injected in the reservoir is greater than the sum of the pressure of the wetting fluid (brine) and the capillary pressure, the non-wetting fluid is likely to enter and flow in the capillary throat whereas if it is lower than that value, the non-wetting fluid is not likely to enter nor flow in that capillary throat. If the entrance and flow of non-wetting fluid occurs, we are talking about a drainage process and if at some point, the pressure of the fluid injected in the reservoir decreases, it may lead to a re-imbibition process.

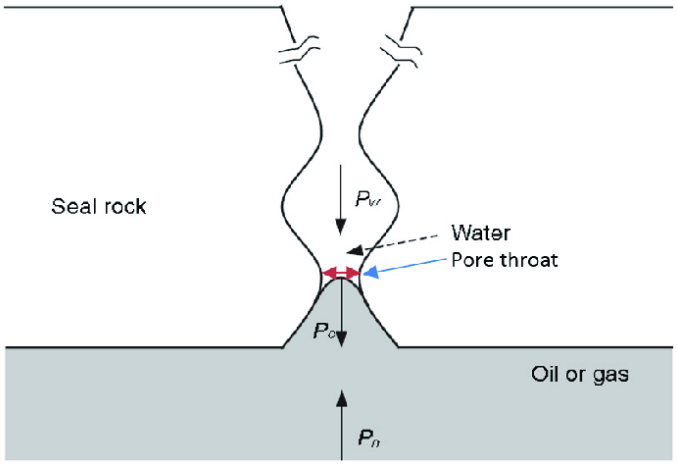

Figure 9: Capillary Sealing Efficiency [21]

The capillary pressure can be expressed as the difference between the pressure of two immiscible fluids (oil – water, gas – water or gas – oil) that exists in the capillaries of the porous media:

$$P_c = P_{nw} - P_w$$ *Equation 4*

P_c: $Capillary\ Pressure$

P_{nw}: $Pressure\ of\ the\ non-wetting\ phase$

P_w: $Pressure\ of\ the\ wetting\ phase$

Another way to express the capillary pressure is:

$$P_c = hg(\rho_w - \rho_{nw})$$ *Equation 5*

h: $Capillary\ rise$

ρ_w: $Density\ of\ the\ wetting\ phase$

ρ_{nw}: $Density\ of\ the\ non-wetting\ phase$

One can also express the capillary pressure with the Young - Laplace equation:

$$P_c = \frac{2\sigma_{nw-w}\cos\theta}{R}$$ *Equation 6*

Where:

P_c: $Capillary\ Pressure\ [Pa]$

σ_{nw-w}: $Interfacial\ tension\ between\ the\ non-wetting\ and\ wetting\ phases$

θ: $Contact\ angle$

R: $Radius\ of\ capillary\ [m]$

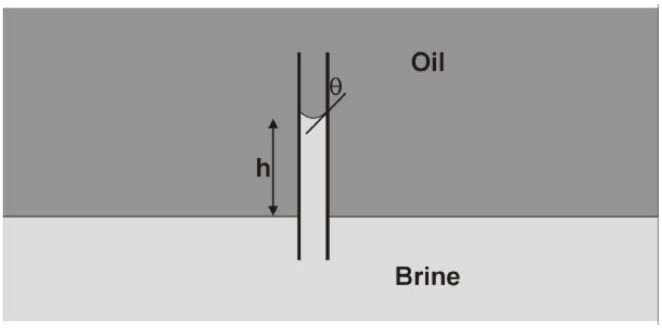

Figure 10: Capillary rise of water in a water wet capillary tube. [18]

The drainage process happens when the wetting phase is displaced by the non-wetting phase (e.g. hydrocarbon migration in geological times in a water wet rock) while the imbibition when the non-wetting phase is displaced by the wetting phase (e.g. waterflooding in a water wet rock).

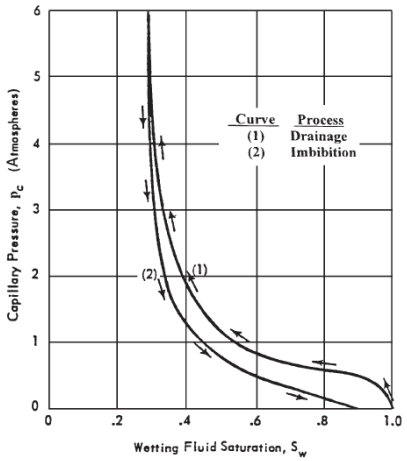

Figure 11: Capillary pressure curves for drainage and imbibition processes. [22]

The difference between the drainage pressure curve and the imbibition pressure curve is due to the hysteresis. The processes may happen in the cap rock of the underground storage if the gas (methane, carbon dioxide or hydrogen) enters and displace the water. Hildebrand et al. illustrated the phenomenon as seen in Figure 12:

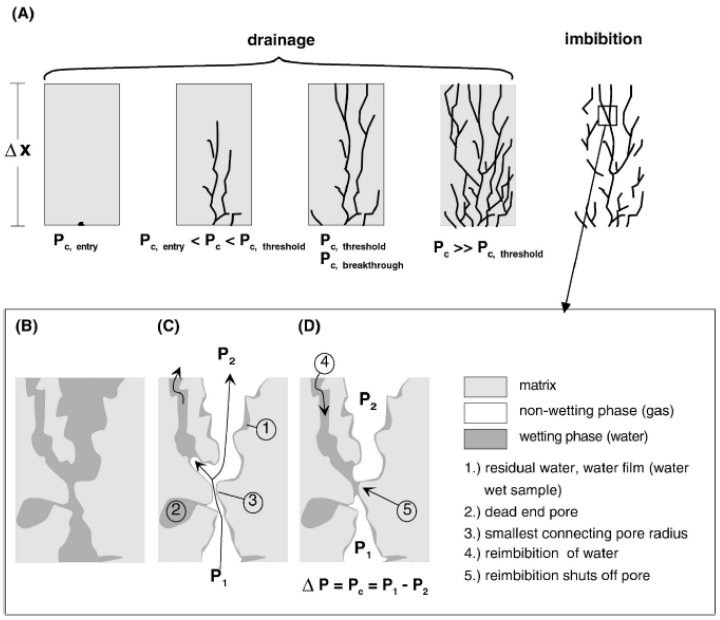

Figure 12: Drainage and Imbibition phenomena in Cap Rocks. [23]

Before the drainage process starts, the cap rock is fully saturated with formation brine as shown in Figure 13 and Figure 14.The drainage process starts when the buoyant pressure exceeds the entry pressure (see Figure 14). At this point, the gas saturation in the cap rock is lower than the critical gas saturation and the result is that the gas phase is being accumulated in the largest non-interconnected pores without flowing since the relative permeability to gas is zero as seen in Figure 13. In the following stage of the process, the buoyance pressure is still greater than the entry pressure but lower than the breakthrough pressure and the gas saturation becomes greater than the critical gas saturation so the gas flows through the cap rock in continuous flow

paths, the gas phase saturation increases, the flow is capillary dominated and there is no flow of non-wetting phase in the downstream. During this stage the relative permeability to water decreases and the relative permeability to gas increases as illustrated in Figure 13. After this, the third stage of the process starts when buoyance pressure is equal to breakthrough pressure, the gas phase arrives to the downstream part of the system through the ***largest of the narrowest capillary pore throat radius*** (i.e. the easiest path). In the last step, the buoyance pressure is greater than breakthrough pressure and the flow becomes viscous dominated and there is a continuous flow of non-wetting phase in the downstream part of the system.

The re imbibition part starts when the buoyance pressure decrease and it becomes lower than the breakthrough pressure. Consequently, the wetting phase naturally spreads over the porous walls and the non-wetting phase saturation decrease up to the residual saturation. This part of the process is illustrated with the red line in Figure 13 and Figure 14. Figure 13 show decrease of the relative permeability to the non-wetting when re imbibition takes part while Figure 14 illustrate that once the residual saturation of the non-wetting phase is reached, the new capillary pressure is called residual pressure difference (i.e. snap-off pressure). As appreciated in Figure 13 and Figure 14, the re imbibition curve does not follow the same path as the drainage curve due to the hysteresis of the system. In consequence, the new state of the system after a drainage and re imbibition process is different from the original state of the system in terms of capillary pressure, relative permeabilities curves and saturation of the fluids.

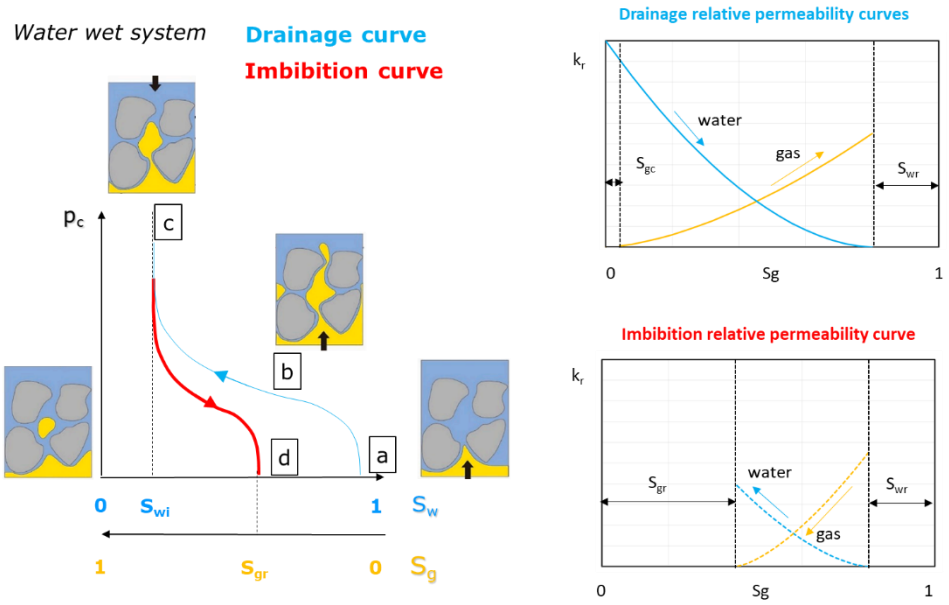

Figure 13: Drainage and imbibition curves [24]

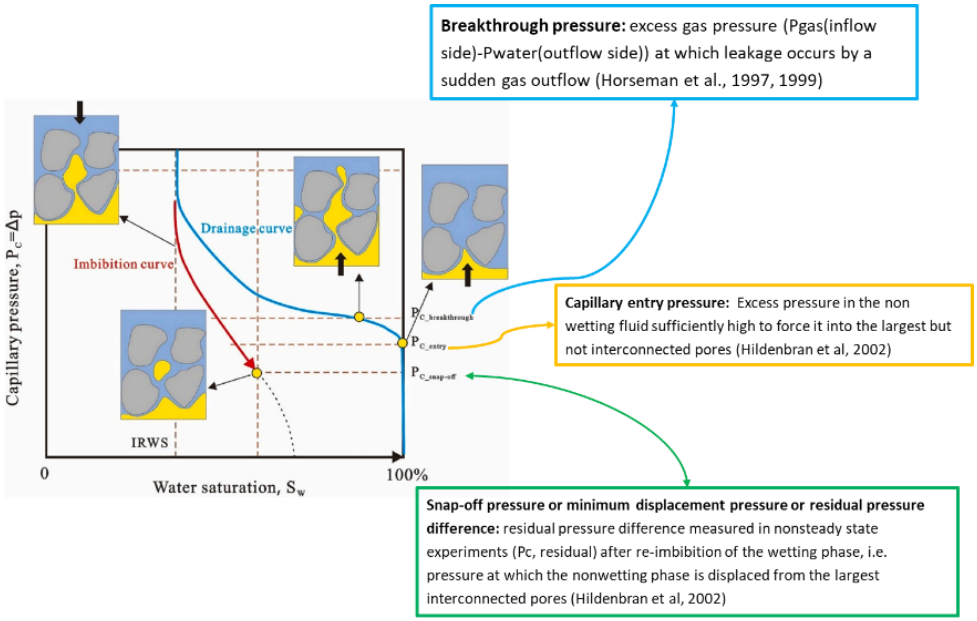

Figure 14: Definitions of Breakthrough pressure, capillary entry pressure and snap-off pressure. [24]

2.1.1. Main factors affecting cap rock sealing efficiency

The sealing efficiency of a cap rock is determined by their properties (e.g. pore throat radius, tortuosity, height) and the interactions between the cap rock, the fluid injected and the brine present in the cap rock. These interactions are governed by factors like wettability (determined by the contact angle) and interfacial tension, which are influenced by subsurface thermodynamic conditions (pressure and temperature).

Since the capillary sealing efficiency depends on the capillary pressure of the rock, one can say that all the factors that affect one, must affect the other. Table 6 show us a list of properties that affects the capillary sealing efficiency and the conditions or parameters that influences each one:

Properties	Conditions/parameters that influences
Difference of densities between wetting and non-wetting phases	Temperature Confining pressure Water salinity Properties of the gas/oil
Interfacial tension between wetting and non-wetting phases	Temperature Confining pressure Water salinity Properties of the gas/oil
Contact angle	Temperature Confining pressure Water salinity Properties of the gas/oil Mineralogy
Capillary radius	Pore size distribution Confining pressure Mineralogy Potential geochemical processes between injected fluids and rocks
Absolute permeability	Pore size distribution Confining pressure

Table 6: Properties that influence in capillary pressure

Influence of confining pressure

As seen in Figure 15, Figure 16 and Figure 17, the ***densities*** of the gases (methane, hydrogen and carbon dioxide) increases with pressure while, as seen in Figure 18, the density of water is almost constant when pressure changes.

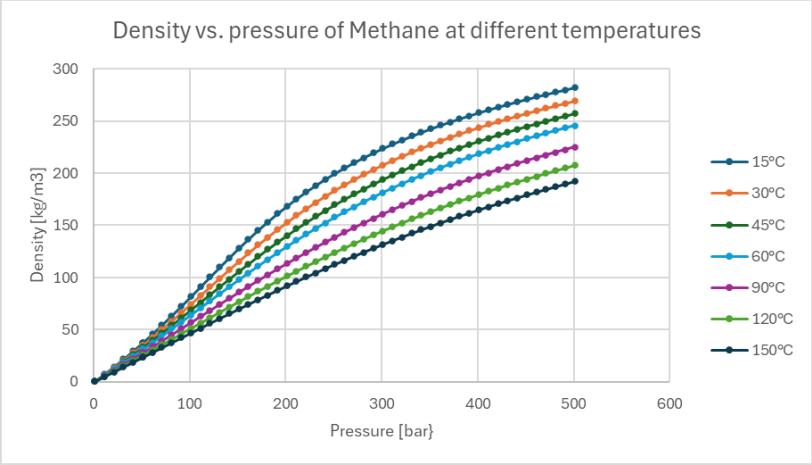

Figure 15: Density vs. pressure of Methane at different temperatures. Data taken from [25]

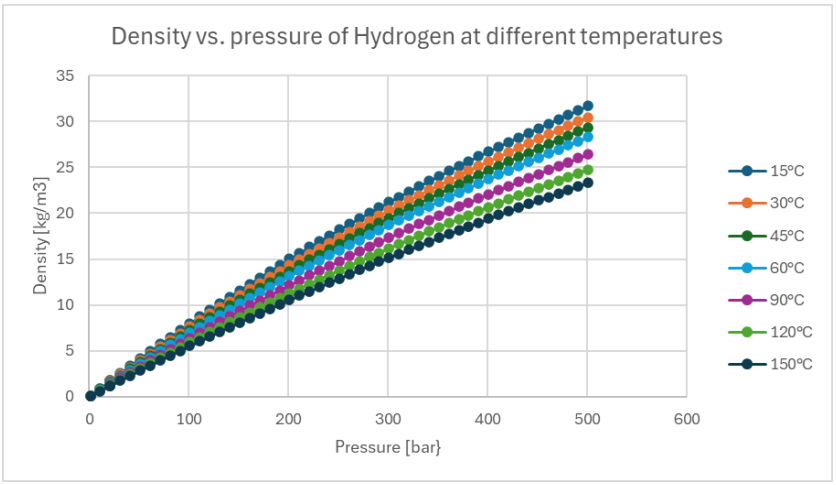

Figure 16: Density vs. pressure of Hydrogen at different temperatures. Data taken from [25]

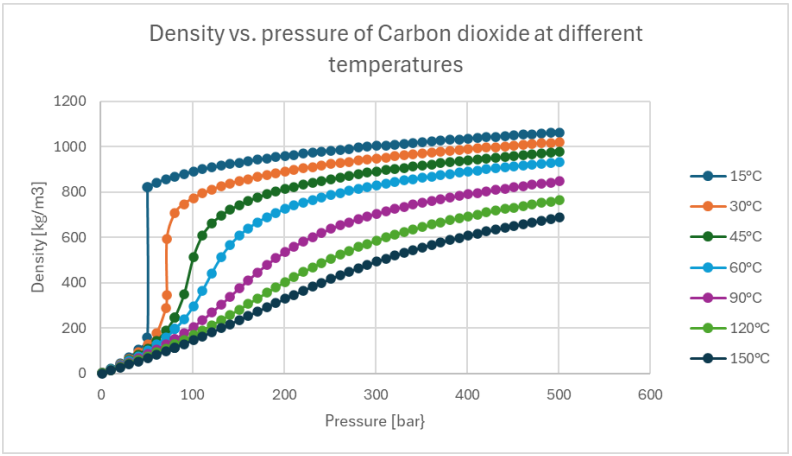

Figure 17: Density vs. pressure of Carbon dioxide at different temperatures. Data taken from [25]

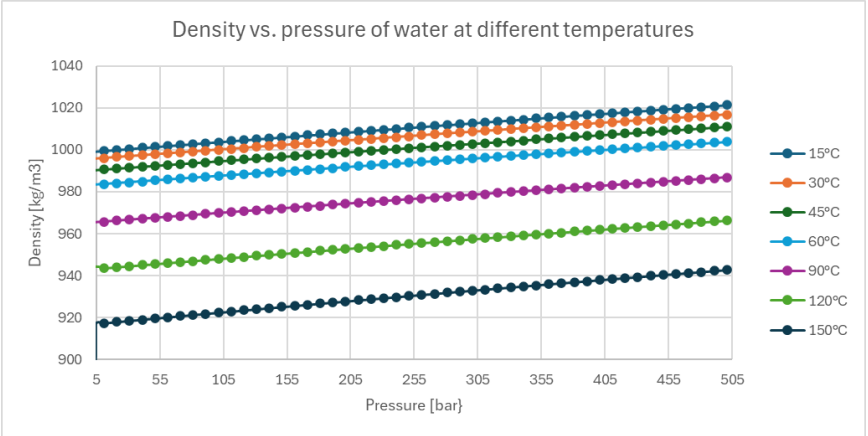

Figure 18: Density vs. pressure of Water at different temperatures, [25]

Mehrjoo et al. [26] analysed the data of ***interfacial tension*** available in the literature for the mixture water – methane at different temperatures, pressures and water salinities. The values of pressure range from 0.1 bar to 2600 bar. the authors found an inverse relationship between pressure and interfacial tension (the higher the pressure, the lower the interfacial tension) below 176°C, then, there is a plateau at 400 bar and above 176°C the data show an inflexion point where the interfacial tension start to increase with pressure at 1000 bar (see Figure 19).

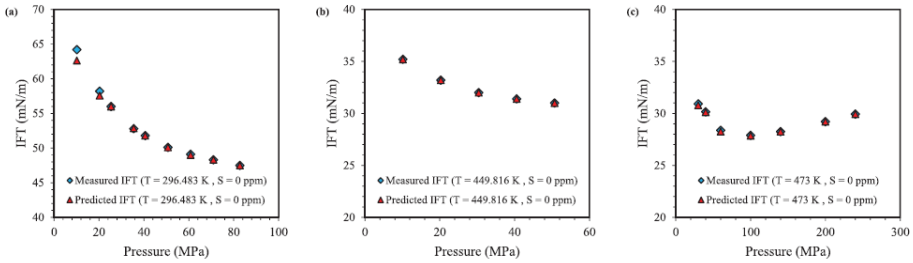

Figure 19: Interfacial tension vs. pressure at different temperatures in water – methane systems. [26]

Hosseini and Leonenko [27] analysed data (153 samples) of interfacial tension in a Hydrogen-Brine system available in the literature. The range of pressures evaluated was from 10 bar to 452 bar. The authors found that the interfacial tension usually increased when pressure decreased. This tendency is also found in the study of Hosseini et al. [28] (Figure 20).

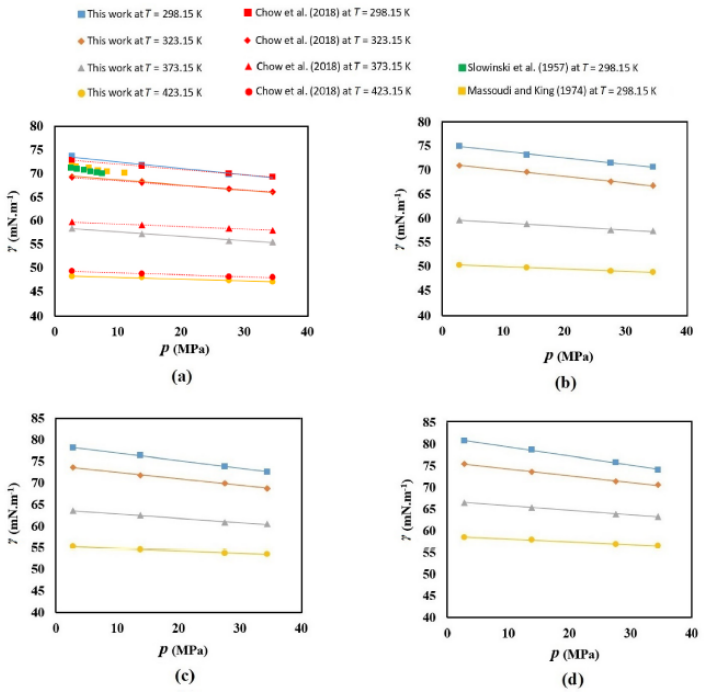

Figure 20: Interfacial tension vs. pressure at different temperatures in a Hydrogen – Brine system. [28]

Chalbaud et al. [29] and Chiquet et al. [30] found on their experiments that in a CO_2-brine mixture, for a constant temperature and salinity, the interfacial tension decreases while the pressure increases until a plateau. They experimented with a range of pressures from 27 to 100 bar [29] and 50 to 450 bar [30].

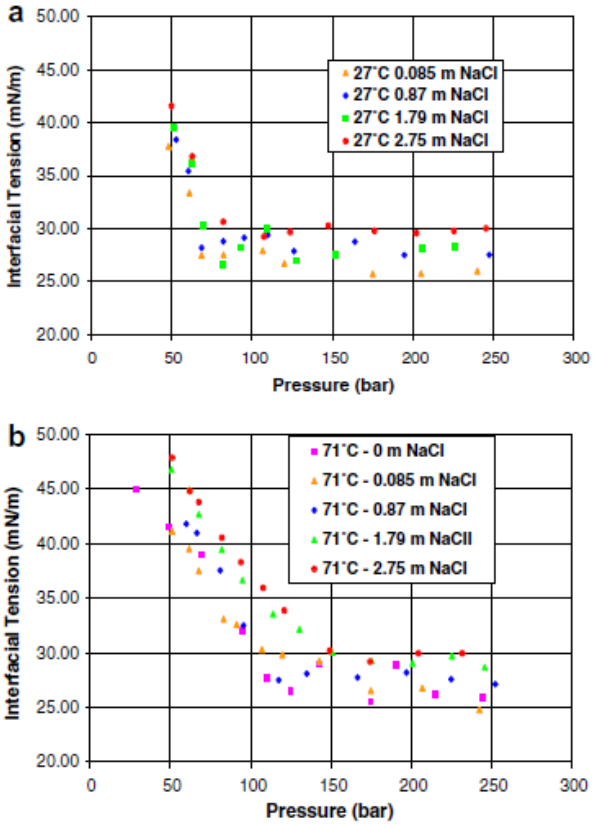

Figure 21: Interfacial tension vs. Pressure at different salinities and temperatures for a CO2-brine system. [29]

When it comes to ***contact angle***, according to the experiments pursued in a carbonate – rich cap rock by Tonnet et al. [31], there is no appreciable variation in contact angle with respect to pressure (in a range from 10 to 140 bar) in a CO_2 – brine system. See Figure 22.

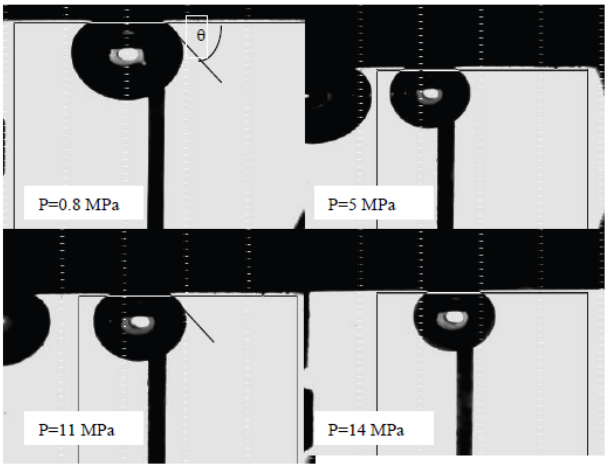

Figure 22: Contact angle of a CO2 – brine system measured at 140°C and different pressures. (29° at 8 bars, 33° at 50 bars, 31° at 110 bars and 29° at 140 bars) [31]

Bikkina [32] also pursued some experiments to measure the influence of pressure and temperature of a $CO_2 - water$ mix in a quartz and a calcite system. The range of pressures applied was 14 to 207 bar. The author found a small increase in the contact angle up to 55°C and after reach liquid/supercritical conditions, a small decrease with pressure.

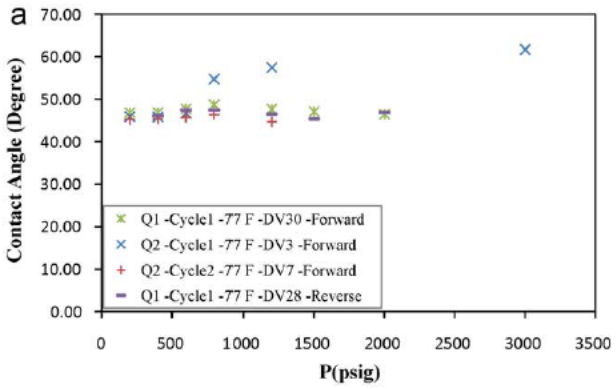

Figure 23: Contact angle at different pressures and 25°C in quartz. [32]

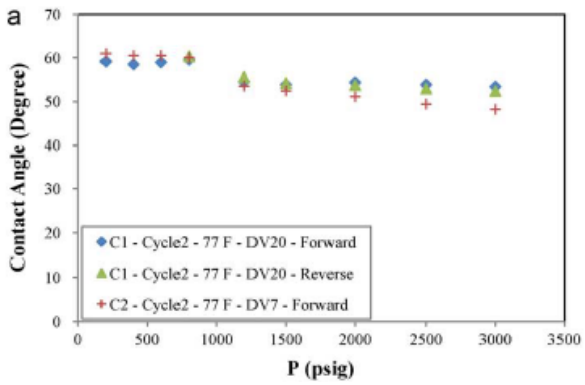

Figure 24: Contact angle at different pressures and 25°C in calcite. [32]

As a conclusion, one can see that in both experiments a small increase in contact angle with pressure is obtained before CO_2 reached liquid/supercritical conditions and a small decrease after this point. Even if these changes are almost negligible according to Tonnet et al. [31].

Deng et al. [33] investigated the behaviour of the ***capillary radius*** for different pressure conditions in a saturated sandstone planned to be used as a reservoir for energy storage. The authors applied 50 cycles of loading and unloading (injection and withdraw) and obtained the results presented in Figure 25. As seen, the stress affected directly the pore size distribution reducing the number of macropores and increasing the number of mesopores and micropores.

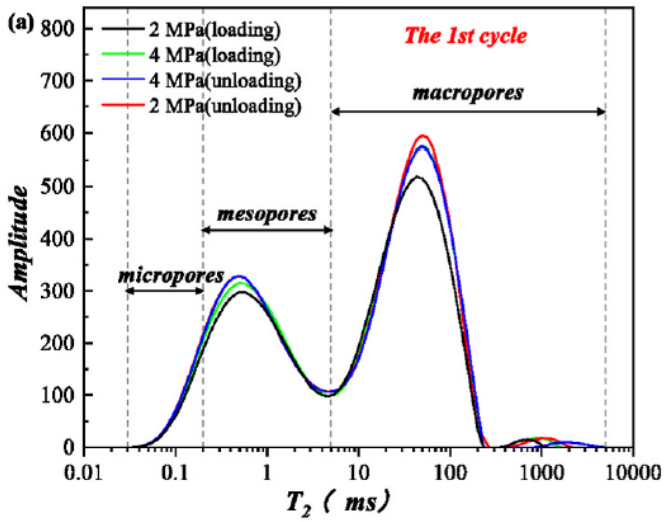

Figure 25: Pore size distribution after the first cycle of loading and unloading. [33]

Influence of temperature

As seen in Figure 15, Figure 16 and Figure 17, the ***densities*** of the gases (methane, hydrogen and carbon dioxide) and the density of water (Figure 18) decreases when temperature increases.

Mehrjoo et al. [26] analysed the data of ***interfacial tension*** available in the literature for the mixture water – methane at different temperatures, pressures and water salinities. The values of temperature range from 5°C to 204°C. the authors found an inverse relationship between temperature and interfacial tension (the higher the temperature, the lower the interfacial tension.

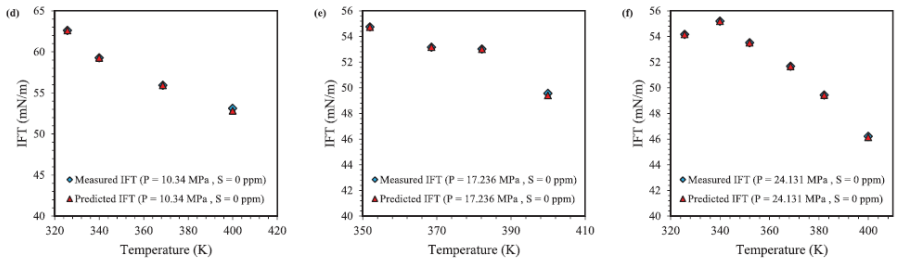

Figure 26: Interfacial tension vs. temperature at different pressures for a methane-water system. [26]

Hosseini and Leonenko [27] analysed data (153 samples) of interfacial tension in a Hydrogen - Brine system available in the literature. The range of temperatures evaluated was from 25°C to 175°C. The authors found that the interfacial typically decrease as the temperature increase. This tendency is also found in a study the study of Hosseini et al. [28]

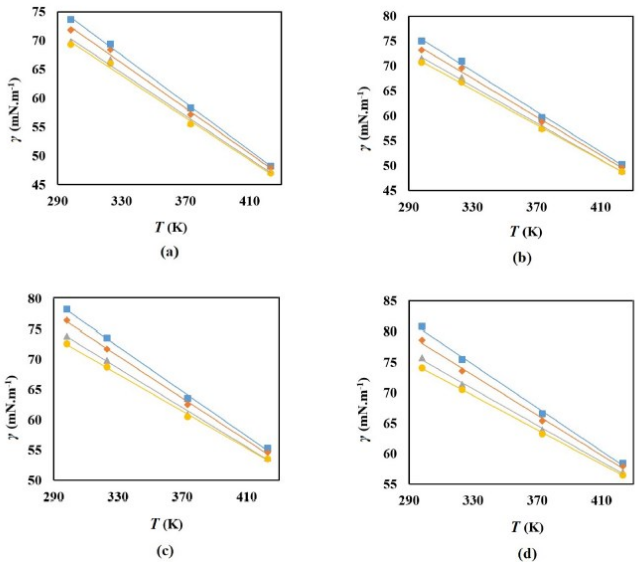

Figure 27: Interfacial tension vs. temperature at different pressures for a Brine – Hydrogen system. [28]

Chalbaud et al. [29] and Chiquet et al. [30] found on their experiments that in a CO_2-brine mixture, for a constant pressure (before a plateau) and constant salinity, the interfacial tension increases while temperature increases before. As seen in Figure 28, for temperatures higher than this plateau, this behaviour is not well defined. The authors worked with a range of temperatures of 48 to 258 °C [29] and 35 to 110 °C [30].

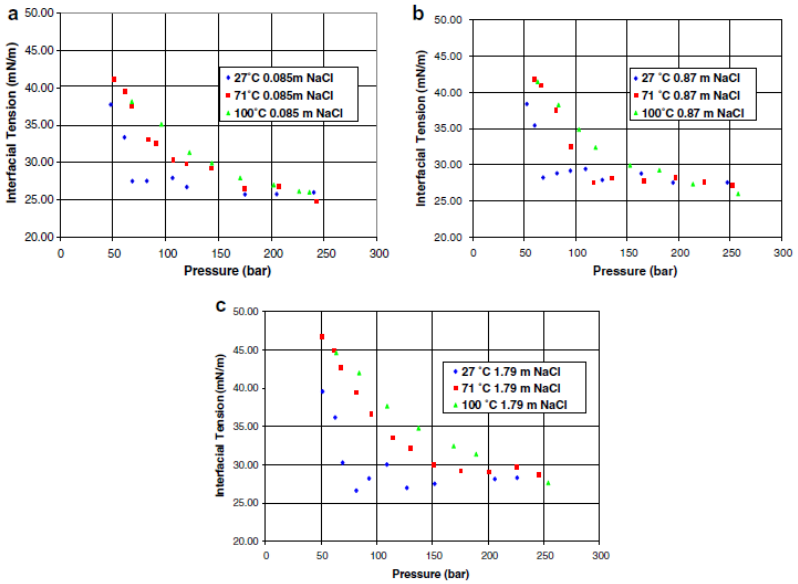

Figure 28: Interfacial tension vs. pressure for different salinities and temperatures. [29]

Regarding the influence on the ***contact angle***, according to the experiments pursued in a carbonate – rich cap rock by Tonnet et al. [31], there is no appreciable variation with respect to temperature (in a range from 35 to 140 °C) in a CO_2 – brine system.

Influence of the properties of the fluid injected

As seen in Figure 29 for all the pressures and temperatures at reservoir conditions, the gas with the highest density (between the gases analysed to store) is CO_2 while the least dense is H_2.

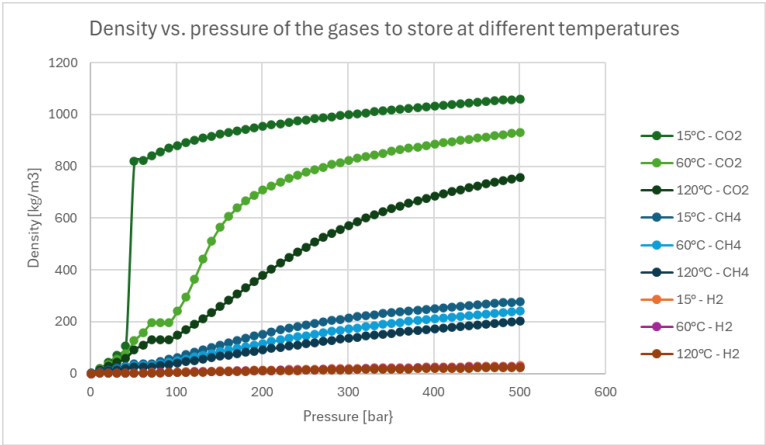

Figure 29: Density vs. pressure of the gases stored at different temperatures. [25]

Mehrjoo et al. [26] analysed the data of interfacial tension available in the literature for the mixture Brine – methane at different temperatures (5°C to 204°C), pressures (0.1 bar to 2600 bar) and Brine salinities (0 to 200000 ppm). The values range from 10mN/m to 76.6 mN/m.

Hosseini and Leonenko [54] analysed data of interfacial tension in a Hydrogen-Brine system available in the literature (153 samples) at different temperatures (25°C to 175°C), pressures (10 bar to 452 bar) and brine salinities (0 to 290000 ppm.). The range of values obtained was from 43mN/m to 70 mN/m.

Chalbaud et al. [29] and Chiquet et al. [30] experiment on carbon dioxide – brine systems with a range of pressures (27 to 100 bar [29] and 50 to 450 bar) [30], temperatures (48 to 258 °C [29] and 35 to 110 °C) [30] and salinities (5000 to 161000 ppm [29] and 0 and 20000 ppm) [30]. They found a range of interfacial tension from 25 to 48 mN/m [29] and 23 to 46 mN/m [30].

Influence of water salinity

From the study of Mehrjoo et al. [26], one can see that ***water salinity*** has a low impact on interfacial tension in methane – brine systems compared to temperature and pressure (see Figure 30). The salinities analysed in the paper range from 0 to 200000 ppm. Whereas according to [34], there is a positive linear relationship between the salinity in brine and the interfacial tension.

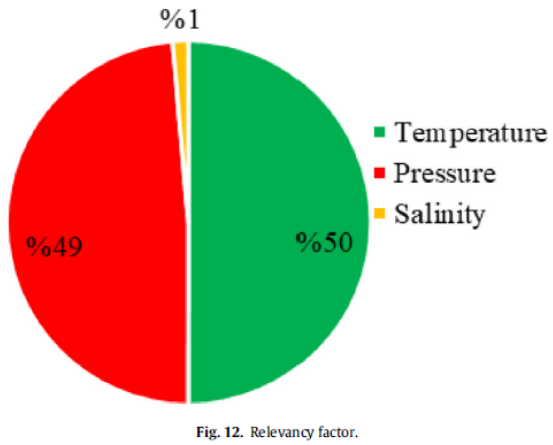

Figure 30: Relevancy factor of temperature, pressure and salinity in interfacial tension for methane – brine systems. [26]

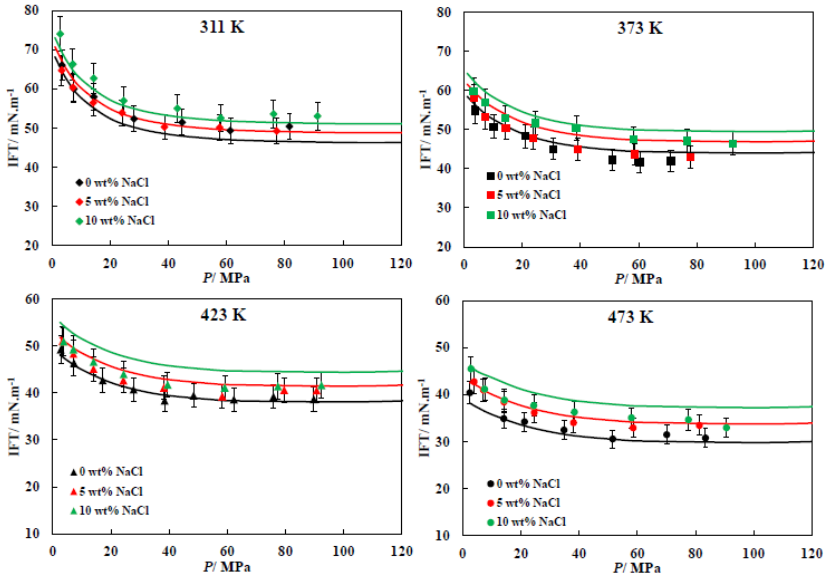

Figure 31: Influence of salinity in the interfacial tension of a brine – methane system at different temperatures and pressures. [34]

Hosseini et al. [28] pursued experiments evaluating the effects of temperature, pressure and brine salinity in interfacial tension in a Hydrogen-Brine system. The salinities analysed in the paper range from 0 to 290000 ppm. The authors found that interfacial tension increases linearly as salinity increases.

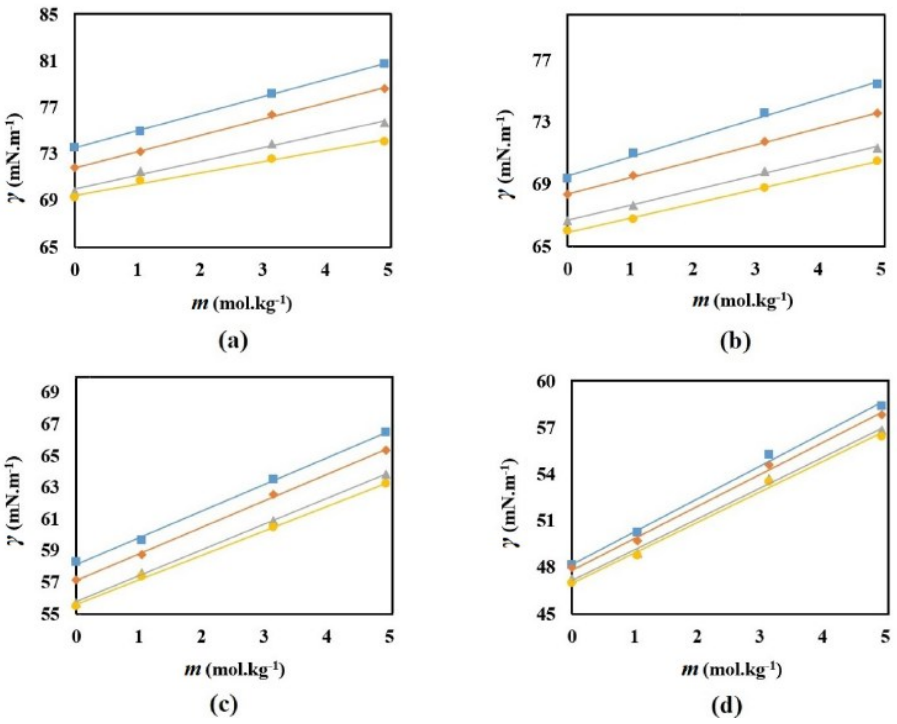

Figure 32: Interfacial tension vs. Brine salinity in a Brine – Hydrogen system at different pressures and temperatures. [28]

Chalbaud et al. [29] found on their experiments that in a CO_2-brine mixture, there are positive linear relationships between the salinity and the interfacial tension. The experiments were pursued in a range of salinities of 5000 to 161000 ppm. As seen in Figure 33, before the plateau, the slope of the relationship depends on the temperature while after the plateau, there is only one slope in the relationship.

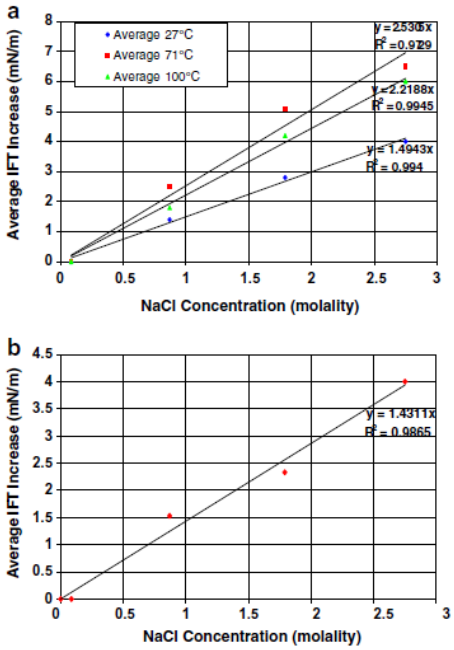

Figure 33: Interfacial tension vs. Salinity at different temperatures. Image a: Before reaching a plateau (see Figure 21). Image b: After reaching a plateau.

Thermodynamic behaviour for different gases

It is important to establish the thermodynamic conditions for storage since, as we seen in the previous paragraphs, they influence directly in the capillary pressure.

Typical initial conditions in saline aquifers are hydrostatic gradient of pressure (0.1 bar per meter) and average geothermal gradient in sedimentary basins (25 – 30°C per kilometre). According to the phase diagram of carbon dioxide seen in Figure 34, the best candidates for storage of carbon dioxide (CO_2) are aquifers between 800 and 1000 meters of depth. [35]

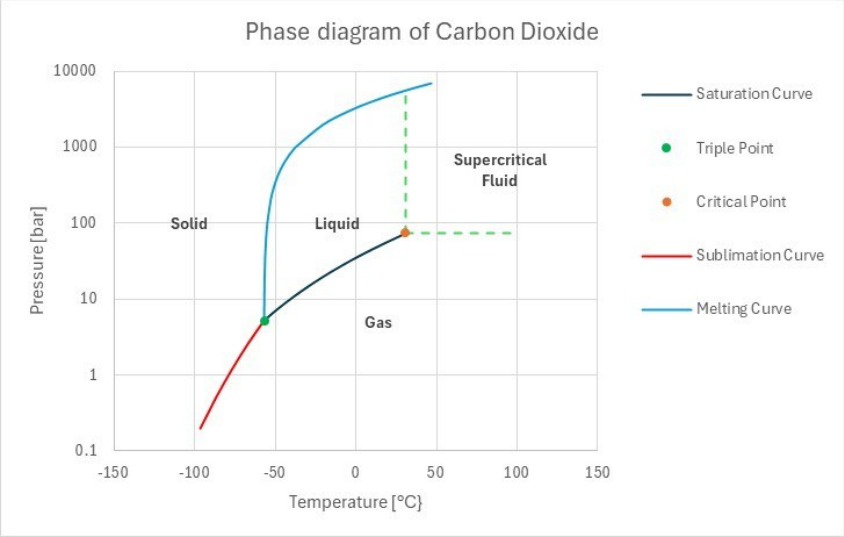

Figure 34: Phase diagram of Carbon Dioxide. Data taken from [25]. Melting Curve done with the Simon–Glatzel equation. Sublimation Curve done with the Clausius–Clapeyron equation.

On the other hand, the typical conditions of storage in depleted oil and gas reservoirs may vary from reservoir to reservoir but in general, the initial pressure is below the original pressure (usually hydrostatic pressure) and it increases with the injection of the gases while the temperature usually follows the average geothermal gradient in sedimentary basins (25 – 30°C per kilometre).

Considering the phase diagram of methane (CH_4) and hydrogen (H_2) seen in, we can see that almost any reservoir deeper than 150m for hydrogen and 500m for methane is suitable for storage of these fluids, depending on the petrophysical properties.

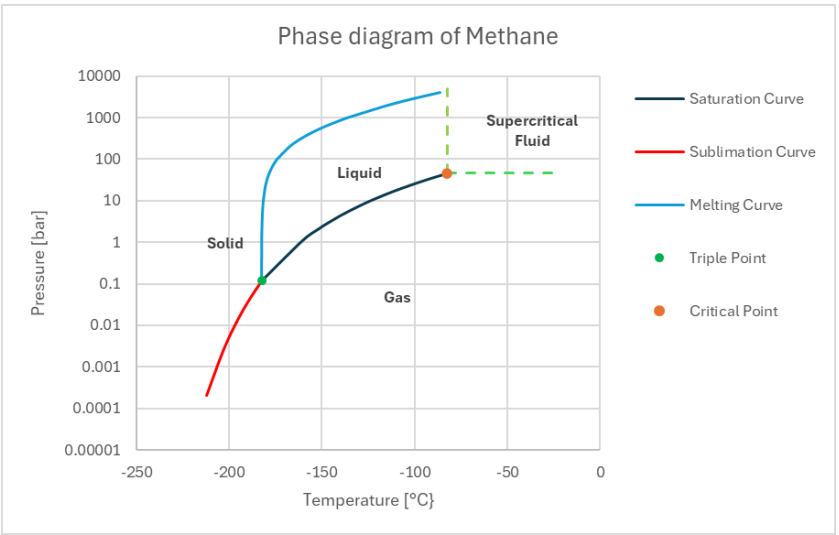

Figure 35: Phase diagram of Methane. Data taken from [25]. Melting Curve done with the Simon–Glatzel equation. Sublimation Curve done with the Clausius–Clapeyron equation.

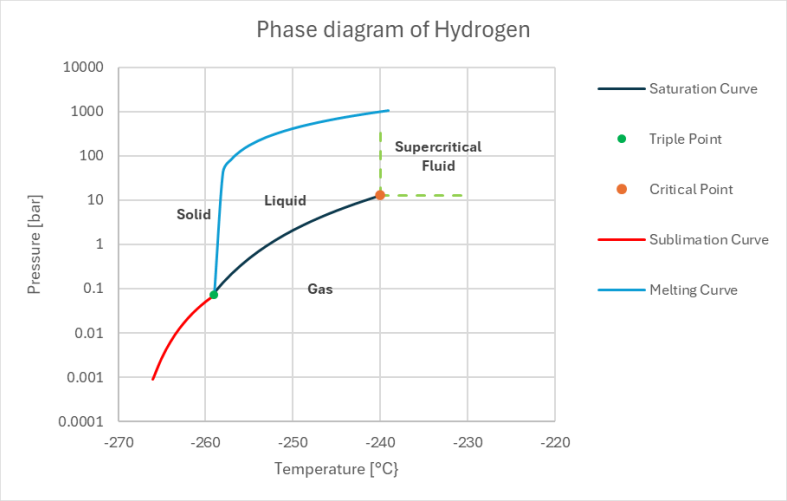

Figure 36: Phase diagram of Hydrogen. Data taken from [25]. Melting Curve done with the Simon–Glatzel equation. Sublimation Curve done with the Clausius–Clapeyron equation.

2.1.2. Laboratory test for the experimental determination of the cap rock sealing efficiency

Although various laboratory tests are available in the literature, there is still no consensus on a standard procedure for determining the breakthrough pressure. In this section, different tests are presented and explained, each one try to reproduce a particular phenomenon that may occurs in the cap rock. Starting from the mercury injection porosimeter test that can be used to obtain a quick estimation of the sealing efficiency of the cap rock, continuing with the standard test (i.e. step by step test) that reproduce the drainage phenomena in which the non-wetting fluid displaces the wetting fluid of the cap rock, then the residual capillary pressure test that, reproducing the drainage and re imbibition phenomena, gives the snap-off pressure is presented and, finally, the dynamic threshold pressure test, an innovative method introduced to obtain the capillary entry pressure in a rapid way with high accuracy, according to the authors.

2.1.2.1. Mercury injection porosimeter test

This test is presented in the paper of W. R. Purcell. [36]. The main objective of this test is obtaining the capillary pressures at each saturation using mercury as nonwetting phase. As explained later in this section, the interpretations available in the literature for this test allow to give a first approximation of the capillary entry pressure. Figure 37 show a scheme of the equipment used.

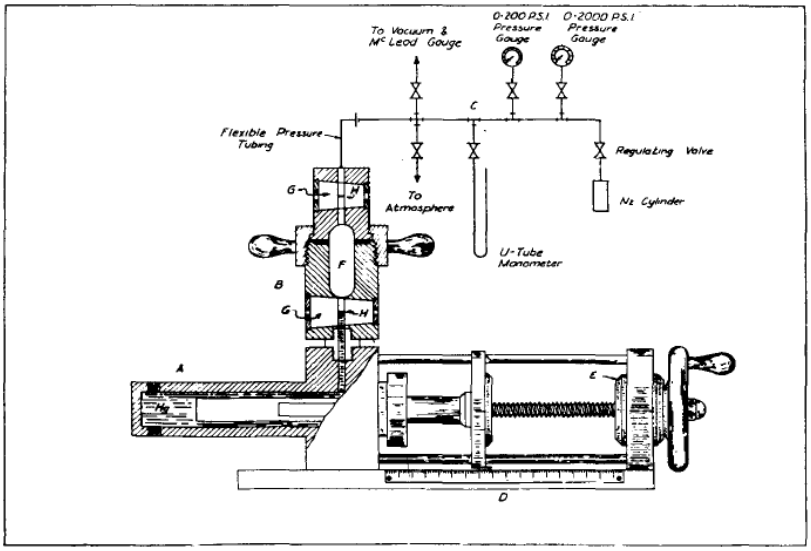

Figure 37: Apparatus for determining Mercury Capillary Pressures [36]. The parts of this apparatus are A: Mercury displacement pump, B: Sample holder, C: Manifold system, D: Scale, E: Vernier, F: Cavity of the sample holder, G: Lucite window, H: Reference marks

Procedure:

- The test starts placing the plugs (or drill cuttings) previously dried in the cavity of the sample holder. Then, the sample holder is filled with mercury and the bulk volume of the sample is obtained.
- No confining pressure is applied.
- Then, the pressure inside the sample holder is increased making that the mercury enters the pores, and a saturation value is determined at each pressure step.
- According to the paper, the entire saturation curve can be reached in 30 to 60 minutes.

A curve of capillary pressure vs. mercury saturation is obtained. Then this curve should be corrected to pass from a mercury – air system to the desired system using the Young-Laplace equation (Equation 6 Equation 6) but modified (in this case for a water – air system but it can be applied for other fluids):

$$R = \frac{2\sigma_{hg-air}\cos\theta_{hg-air}}{P_{c_{hg-air}}} = \frac{2\sigma_{air-water}\cos\theta_{air-water}}{P_{c_{air-water}}}$$

Or:

$$\frac{\sigma_{hg-air}\cos\theta_{hg-air}}{P_{c_{hg-air}}} = \frac{\sigma_{air-water}\cos\theta_{air-water}}{P_{c_{air-water}}} \qquad \textit{Equation 7}$$

Special attention should be taken to the values obtained using this test since, as previously explained, the procedure is performed using a mercury – air system under certain conditions of pressure and temperature and the correction done with Equation 7 uses theoretical values of

interfacial tension and contact angle available in the literature. This method is commonly used as a first estimation rather than a precise value.

Some interpretations of the data are available in the literature. The tangent method states that the pore entry pressure is given by the tangent to the plateau of the mercury intrusion curve, as seen in Figure 38, another interpretation often used points that the capillary entry pressure is obtained at the pressure at which the 10% of mercury saturation is reached, as shown in Figure 39.

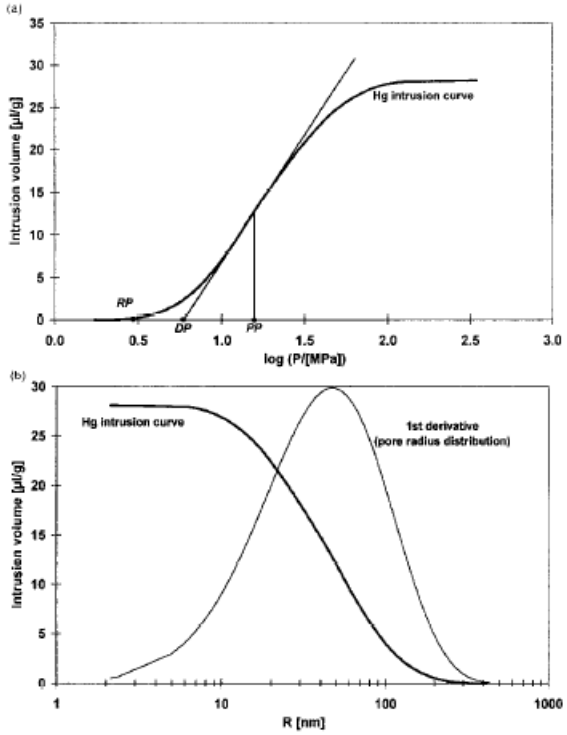

Figure 38: Interpretation of the Mercury injection porosimeter test data. [37]

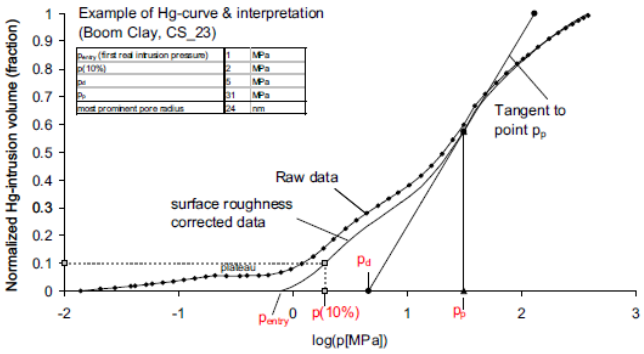

Figure 39: Interpretation of the data from a Mercury injection porosimeter test to obtain the capillary entry pressure of the cap rock. [38]

2.1.2.2. Standard test – Step by Step test

This test was introduced in the paper of Thomas et al. [39]. The purpose of the procedure is to replicate the drainage process in the cap rock and obtain a value of breakthrough pressure measured directly from the core sample and using in situ conditions. The procedure is the following:

- Preparation of the sample
  - Saturation of cores with distilled deaerated water containing 25 ppm $HgCl_2$.
  - Dry the cores in an oven at 104.4 °C (220 °F) for 24 hours.
  - Saturate the core with CO_2 passing several pore volumes of the substance through the core.
  - Evacuate the sample for 12 hours.
  - Flood the core with deaerated water.
  - Put the sample in a water pressure chamber at 69 bars (1000psia) for a period to fully saturate it with water.
- Put the core sample into the core holder.
- Apply a pressure between 69 and 103.4 bar (1000 to 1500 psia) to the sleeve of the core holder (confining pressure).
- Apply gas pressure to the bottom of the core holder in small steps determined by the permeability of the core. The lower the permeability, the larger the pressure increment.
- Read the water flow in the outlet in each increment.
- The breakthrough pressure is reached when a continuous flow of water appears in the outlet and, if enough time is allowed, gas finally appears.

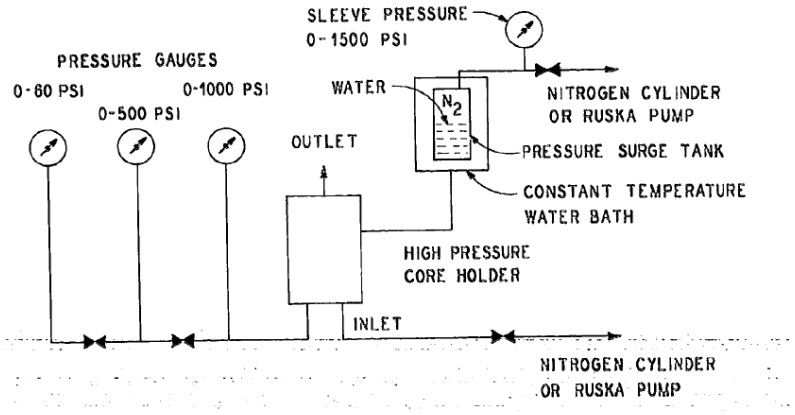

Figure 40: Schematic flow diagram of the High-Pressure Core Holder apparatus. [39]

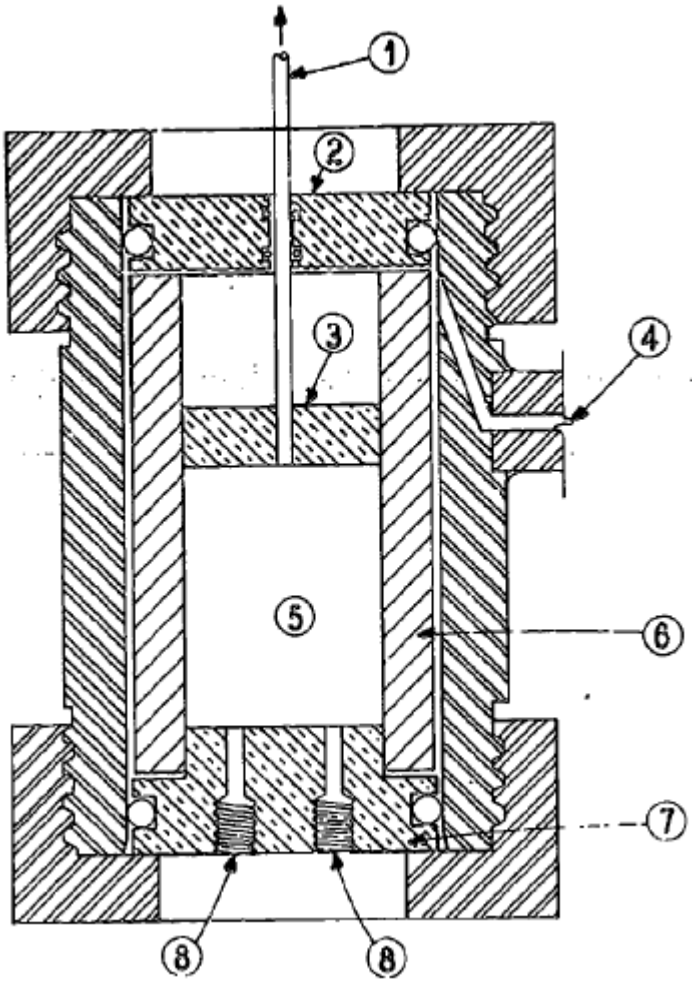

Figure 41: High Pressure Core Holder for Standard Test. [39]. The parts of the apparatus are: 1: Outlet stem, 2: Top Core Holder end plate, 3: Top Core Sample end plate, 4: Pressure inlet for rubber sleeve, 5: Core Sample, 6: Rubber Sleeve, 7: Bottom Core Holder and Sample end plate, 8: Gas or water inlets

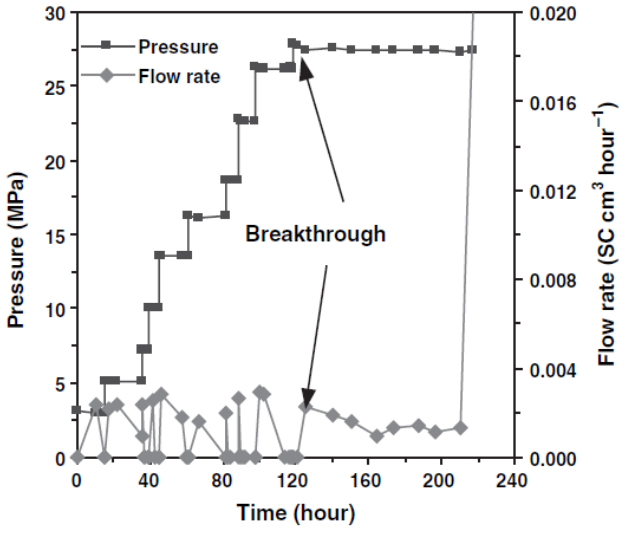

Figure 42: Data obtained from a standard test. [40]

2.1.2.3. Residual capillary pressure test – Snap-off test

The concept of residual capillary pressure is briefly introduced by Thomas et al. [39] in their paper as a new threshold pressure after resealing of the sample lower than when the sample is a 100% saturated with water. This concept was later taken by Hildebrand et al. [23] as "pressure at which the nonwetting phase is displaced from the largest interconnected pores".

The experiment simulates the processes of drainage (displacement of water by gas) and re-imbibition (displacement of gas by water) of the cap rock to finally obtain a value of residual capillary pressure (snap-off pressure). A scheme of the equipment used is shown in Figure 44. The procedure is the following:

- Fully water/brine saturated plugs are placed between two porous stainless-steel disks and two stainless steel pistons equipped with boreholes for fluid introduction and removal.
- Apply confining pressure higher than the expected gas breakthrough pressure to avoid hydrofracturing.
- Apply an instantaneous high-pressure gradient (exceeding the expected gas breakthrough pressure), to force gas breakthrough.
- Then, as seen in Figure 43, there are 2 different procedures to perform the experiment:
    - Procedure A: The upstream (high-pressure) side of the cell is kept at a constant pressure by means of a pressure regulator.
    - Procedure B: The upstream (high-pressure) side of the cell filled with gas at high pressure and then sealed.
- The system is close therefore over time, the pressure difference across the sample is expected to decline until it stops completely (i.e. gas flow is interrupted) as showed in Figure 43. The pressure difference drops causes that the wetting phase start to regain pore space starting with smaller pore, until it completely traps the gas phase within the pore system. The final pressure difference (after stabilization) is the residual pressure (snap-off pressure).

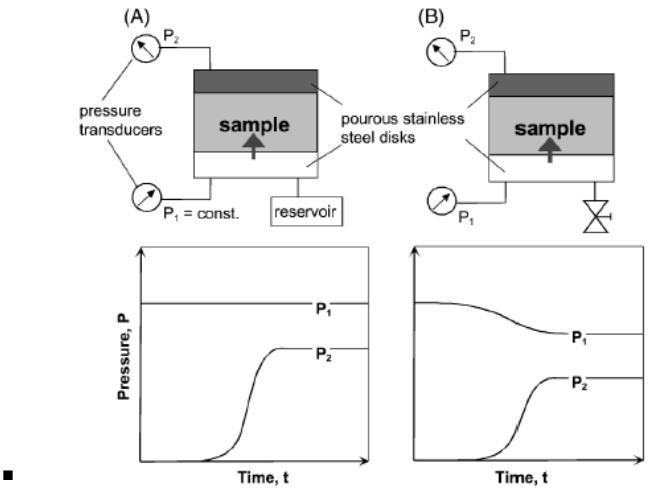

Figure 43: Scheme of the two experimental modes. (A) constant pressure at upstream side; (B) introduction of gas into a fixed upstream volume; downstream volume fixed in both instances. [23]

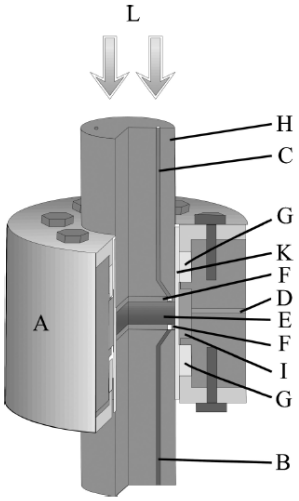

Figure 44: Triaxial flow cell used for single-phase permeability measurements and gas breakthrough experiments. Parts of the apparatus: A: Body, B and C: Conduits, D: Connector for confining pressure, E: Rock sample, F: Porous disks, G: Packing material, H: Pistons, I: Confining pressure confinement, K: Double layered sleeve, L: Axial load

An example of data obtained is shown in Figure 45. The conceptual flow of capillary processes in the experiment is shown in Figure 46.

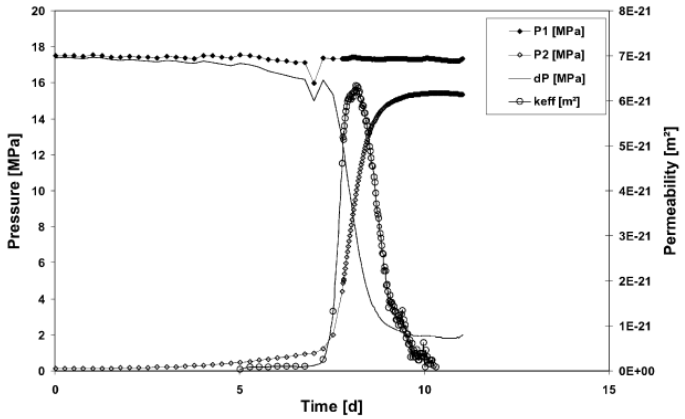

Figure 45: Gas breakthrough curve for methane including the permeability curve calculated. [23]

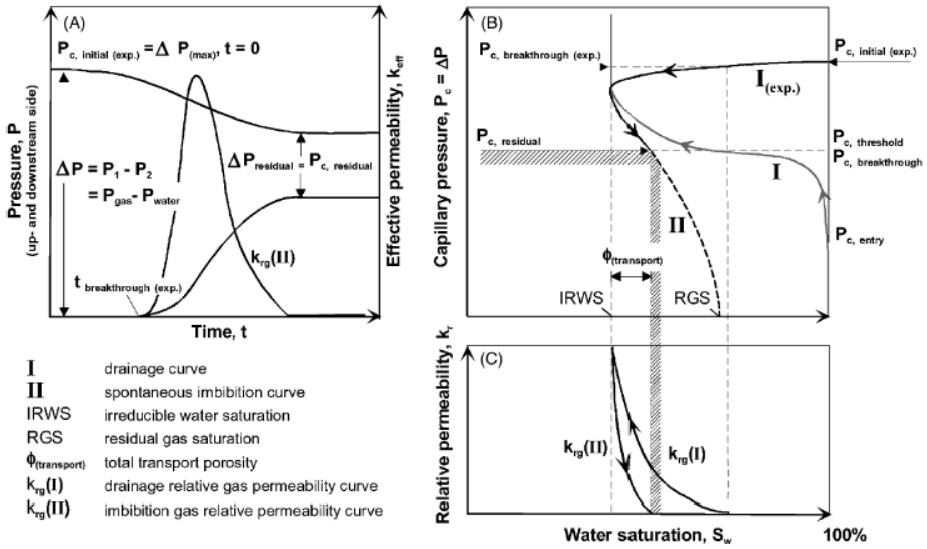

Figure 46: Scheme of the experimental parameters recorded and their interpretation in terms of capillary processes. (A) pressure history of a gas breakthrough experiment; (B) capillary pressure of the gas phase as a function of water saturation. (C) relative permeability curve for the gas phase as a function of water saturation during drainage (I) and imbibition (II).

2.1.2.4. Dynamic threshold pressure test

This method was introduced by Egermann et al [41] to show a method that, according to them, is as accurate as the standard method but much faster. Due to the nature of the experiment, this procedure gives a value of capillary entry pressure. The authors purpose the principle that when the wetting fluid is flowing through the core sample, the difference in pressure between the two extremes (inlet and outlet) of the sample can be calculated using the Darcy law for incompressible fluids rearranged:

$$Q = \frac{KA\Delta P}{\mu L}$$ *Equation 8*

Where:

ΔP: $Pressure\ drop\ [Pa]$

Q: $flow\ rate\ [m^3/s]$

μ: $viscosity\ [Pa * s]$

L: $lenght\ of\ the\ pipe\ [m]$

K: $permeability\ [m^2]$

A: $cross\ sectional\ area\ [m^2]$

When the nonwetting phase starts flowing through the core sample, three zones are generated: Upstream invaded by non-wetting fluid region, the front zone with a with a pressure jump associated with the threshold capillary pressure and the virgin zone with wetting fluid.

They postulated the following pressure profile for the entire core sample:

$$\Delta P_{core} = P_{inlet} - P_{outlet} = \Delta P_{invaded} + \Delta P_{front} + \Delta P_{virgin}$$ *Equation 9*

According to the authors:

- The extension of the invaded zone is so limited at the beginning of the injection that the pressure drop in the invaded zone can be neglected.
- The pressure drop in the virgin zone can be calculated with the Darcy law for incompressible fluids (Equation 8).
- The pressure drops in the front (between the nonwetting and the wetting fluid) is equal to the capillary threshold pressure.

So, we obtain:

$$\Delta P_{virgin} = \frac{Q_w \mu_w L}{KA}$$ *Equation 10*

$$P_{th} = \Delta P_{front} = \Delta P_{core} - \Delta P_{virgin} = P_{inlet} - P_{outlet} - \Delta P_{virgin}$$ *Equation 11*

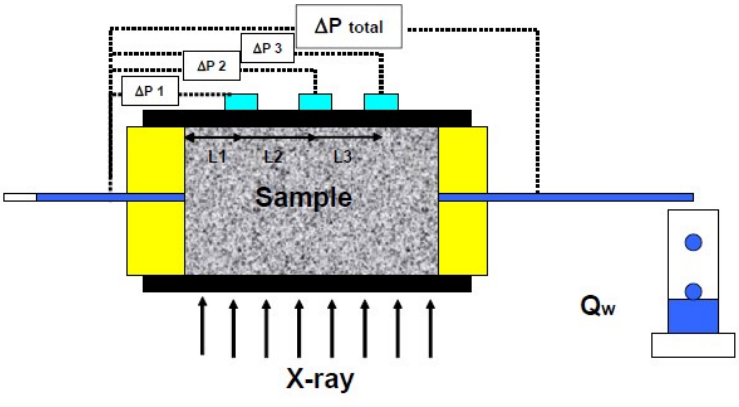

Figure 47: Experimental set up used by Egerman et al. [41]

The authors proposed the following procedure:

- Preparation:
  - Put the core sample in the core holder and impose reservoir conditions (confining pressure and temperature).
  - Inject the wetting fluid into the brine saturated sample at a constant ΔP_t chosen a priori higher than the expected P_{th}.
- First period:
  - Calculate the permeability of the system using the Equation 8 while only the wetting fluid is flowing in the core sample.
- Second period:
  - When the nonwetting fluid starts flowing through the core sample, there is a decrease in the outlet rate (Q_w) due to the P_{th} in the front between the nonwetting and the wetting zones.

The data collected in this experiment are:

- Permeability to water from the first period.
- Breakthrough pressure from the second period.

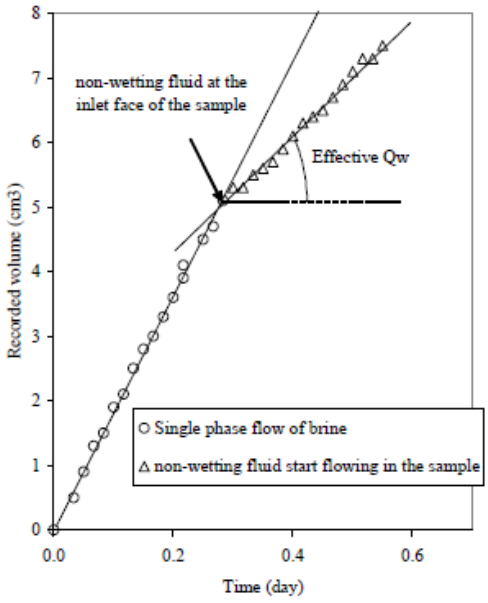

Figure 48: Typical production curve recorded at the outlet. [41]

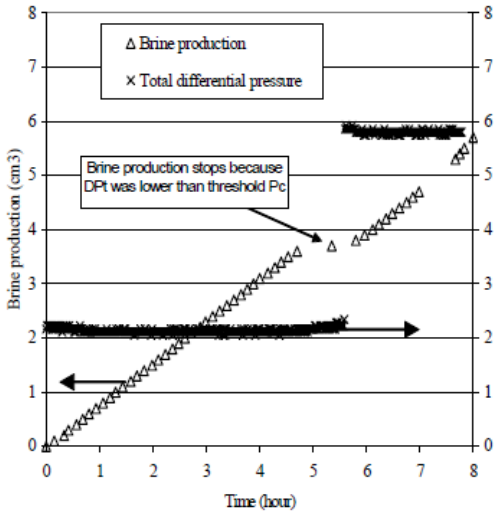

Figure 49: Typical production curve recorded at the outlet when the pressure drop applied is lower than the threshold pressure. [41]

The authors also proposed the implementation of some local measurements of pressure in the core ($\Delta P_1, \Delta P_2$ *and* ΔP_3 in Figure 47) and apply the same equation to each one (Equation 11) to obtain local measurements of threshold capillary pressure taking into account the heterogeneity of the core sample.

Comparison of the laboratory tests available in the literature

As shown during this section, there are four experiments used to evaluate the sealing efficiency of the cap rock. The following table show us a comparison of all the presented approaches:

Name	Value obtained	Advantages	Disadvantages
Mercury Injection	Capillary entry pressure	Relatively fast No need of regular plugs	Indirect estimation No in-situ conditions
Standard test (Step by step test)	Breakthrough pressure	High accuracy In situ conditions Direct estimation of the values	Long test (mainly in rocks with extremely low permeability)
Residual capillary pressure test (Snap-off test)	Snap-off pressure	High accuracy In situ conditions Reproduce the drainage and re imbibition phenomenon	The snap-off pressure is lower than the breakthrough pressure
Dynamic threshold pressure test	Capillary entry pressure	Relatively fast In situ conditions	The capillary entry pressure is lower than the breakthrough pressure

Table 7: Comparison of the laboratory tests available in the literature

From Table 7 can be extracted that the only test that give an accurate value of breakthrough pressure is the standard (step by step) test. Despite this main advantage, one limitation is the time it takes to perform the procedure mainly if no estimated values are available. This limitation can be reduced if other methodologies are implemented to give a first estimation of a potential breakthrough pressure (e.g. mercury injection test, correlations, numerical simulations).

3. Theoretical framework of the multiphase fluid flow in porous media

3.1. Model developed

A model built using the software COMSOL Multiphysics® was used to represent the core samples and the experiments pursued. The model was developed coupling the physics processes of ***Darcy's Law and Phase Transport in Porous Media of the Fluid Flow*** module of the software. The governing equations implemented in the software are the Darcy law for each phase (Equation 12) combined with the conservation equation for each phase (Equation 13)

$$v_i = -\frac{k_{ri} * k}{\mu_i}(\nabla p_i - g\rho_i) \qquad \textit{Equation 12}$$

Where:

v: $velocity$

q: $rate$

A: $cross\ sectional\ area$

k: $permeability$

μ: $viscosity$

∇p: $pressure\ gradient$

g: $gravitational\ constant$

ρ: $density$

i: $phase$

$$\frac{\partial}{\partial t}(\rho_i \emptyset_i) + \nabla(\rho_i v_i) = q_i \qquad \textit{Equation 13}$$

Where:

ρ: $Density$

$\emptyset$: $Porosity$

v: $Velocity\ (From\ Darcy\ equation)$

i: Phase

q_m: $Mass\ source\ term$

The representation is a simplification of the capillary bundle model concept using 20 parallel tubes representing the capillaries of the core sample. The radii distribution of the capillary tubes was obtained from the literature (see Figure 50):

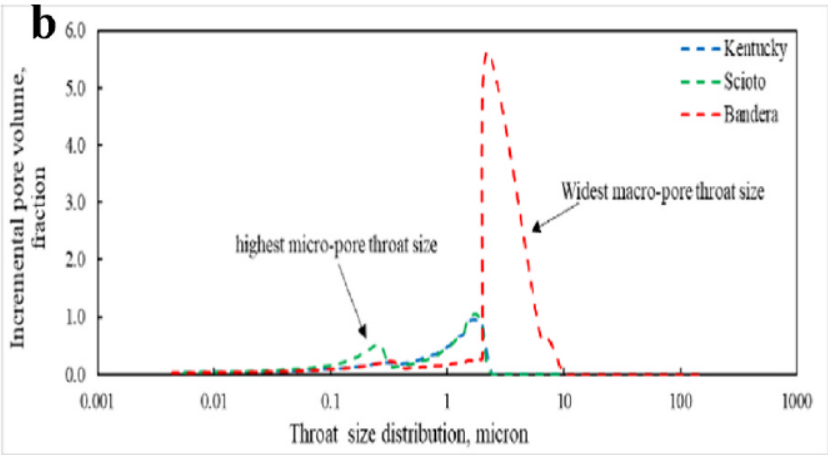

Figure 50: Pore throat size distribution of the Scioto Sandstone. Taken from [42]

The model was built in order that each capillary tube represents a 5% of pore volume, consequently, all the tubes have the same radii; but a different equivalent radius, which means different transport properties.

For each capillary tube, the permeability was obtained from the combination of the Darcy law for incompressible fluids (Equation 8) and the Poiseuille equations (Equation 14):

$$Q = \frac{\pi r^4 \Delta P}{8\mu L}$$ Equation 14

Combining Equation 8 and Equation 14:

$$Q = \frac{k\pi r^2 \Delta P}{\mu L} = \frac{\pi r^4 \Delta P}{8\mu L}$$

Rearranging we obtain:

$$k_{initial} = \frac{{r_{eq}}^2}{8}$$ *Equation 15*

The capillary pressure of each tube was obtained from Equation 6 while the interfacial tension was obtained from the literature as a function of pressure and temperature as showed in Figure 51. The contact angle used was 35°.

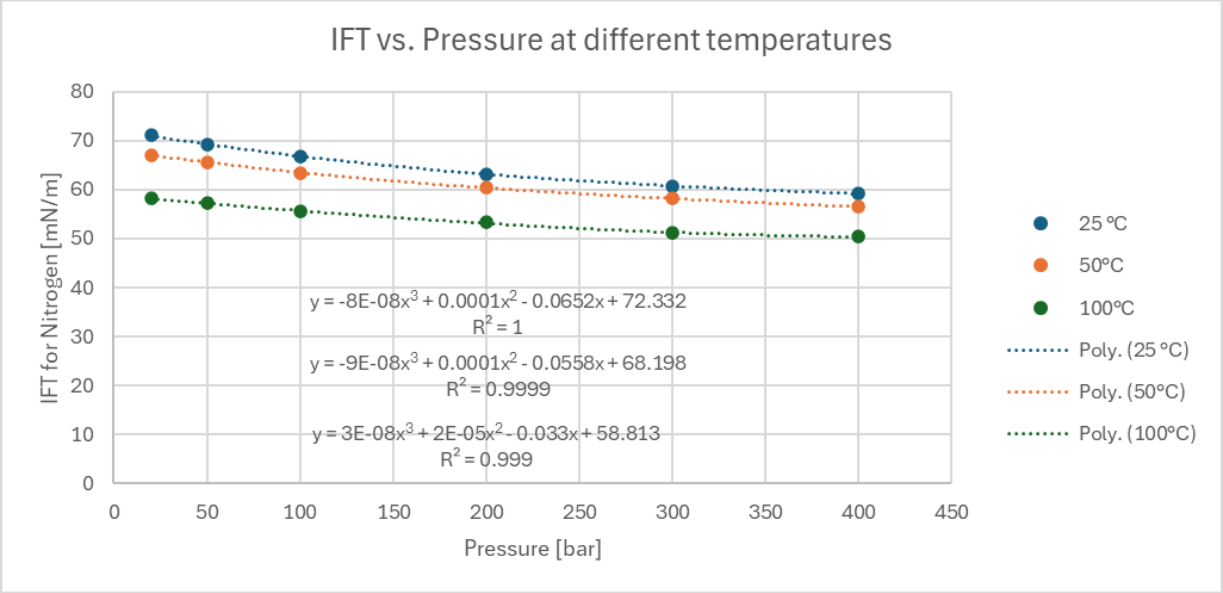

Figure 51: IFT vs. pressure at different temperatures for a Nitrogen – Water system. Data taken from [43]

The model also uses the concept of tortuosity (illustrated in Figure 52) to consider the real path of the capillary tubes affecting the equivalent radius of each capillary:

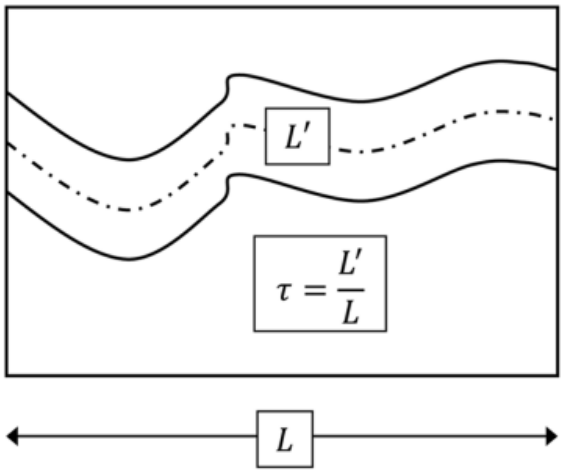

Figure 52: Illustration of tortuosity (τ). Taken from [44]

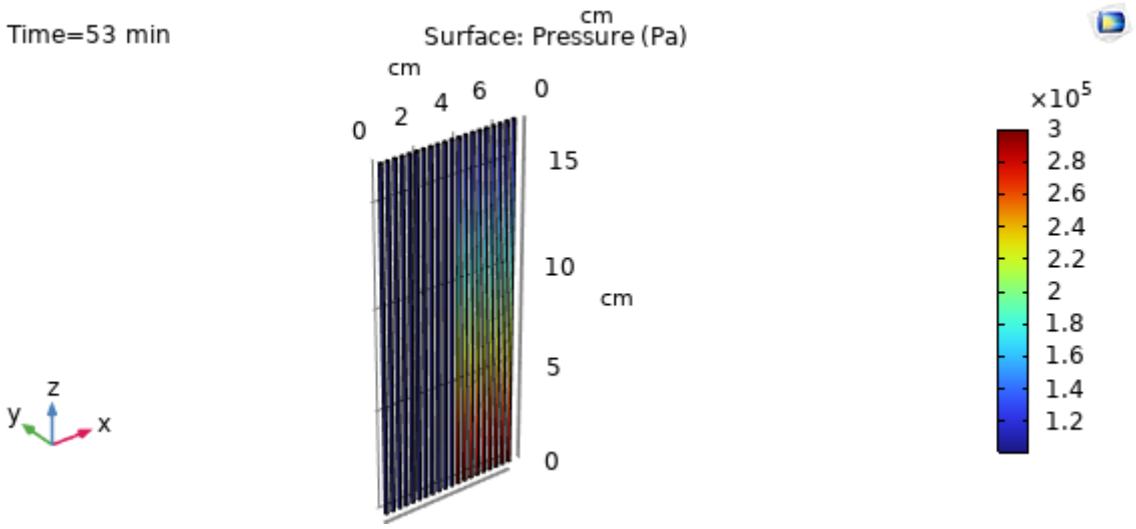

Figure 53: Capillary bundle model generated in COMSOL Multiphysics®

3.2. Main flow phenomena description

According to Ho and Webb [45] the mechanisms of transport of gas in porous media can be divided in advective and diffusive mechanisms. Here, the definition of the Knudsen number is fundamental to difference which are the conditions for each type of flow:

$$k_n = \frac{\lambda}{d} \qquad \textit{Equation 16}$$

Where:

k_n: *Knudsen number*

λ: *mean free path*

d: *pore diameter*

One can, then, divide the transport mechanisms of gas in the following way (Since this classification is empirical, some authors may suggest other limits of Knudsen number to divide certain categories). [45] [46] [47] [48]:

Type	Mechanism	Knudsen number range
Advection	Viscous flow (Darcy flow)	$k_n < 0.001$
	Slip flow (Knudsen flow)	$0.001 < k_n < 0.1$
Diffusion	Transition flow*	$0.1 < k_n < 10$
	Continuum diffusion (Ordinary diffusion)	$k_n < 0.1$
	Knudsen diffusion (Free molecular diffusion)	$k_n > 10$

Table 8: Transport mechanisms classification

* Some authors include a transitional flow between Slip flow and Free molecular diffusion ($0.1 < k_n < 10$) where both types of flow have some influence in the behaviour of the gases.

This work is focused on the advection processes, so we are going to dismiss the diffusion types of mechanisms.

The viscous or Darcy flow occurs when the pore diameter is much greater than the mean free path of the molecule. This type of flow is controlled by a pressure gradient of a continuous fluid mixture (no separation of species). If we assume laminar flow, the viscous flow is described by the Darcy Law (Equation 2) [45]. Considering that the mean free path of the molecule depends on the temperature, pressure and the kinetic diameter of the gas, the type of flow depends on the specific conditions of the site and the type of gas injected.

On the other hand, the Slip flow (Knudsen flow or Klinkenberg effect) occurs when the pore diameter is slightly bigger than the mean free path of the molecule. At these conditions, Klinkenberg [46] described the phenomenon as "if the wall has a zero velocity, then the velocity of the gas layer in the immediate vicinity of the wall has a finite value. Consequently, the quantity of gas flowing through a capillary is larger than would be expected from Poiseuille's formula". The slip flow theory of Klinkenberg account for the modification of the permeability and is described by Equation 17 [46]. As shown, the pressure has an inverse influence on the permeability (i.e. in the velocity of the gas) which means that at high pressures (i.e. reservoir conditions), the Klinkenberg effect is negligible while at low pressures (i.e. laboratory conditions measuring permeability to gas), this effect has an influence in the permeability measurements:

$$k_a = k\left(1 + \frac{4c\lambda}{r}\right) = k\left(1 + \frac{b}{p}\right) \qquad \textit{Equation 17}$$

Where:

k_a: $apparent\ permeability\ (gas\ permeability)$

k: $true\ permeability\ (liquid\ permeability)$

c: $proportionality\ factor$

λ: $mean\ free\ path\ of\ the\ molecule$

r: $pore\ radius$

b: $slippage\ factor$

p: $average\ pressure$

In low-permeability formations, such as cap rocks, capillary pressure plays a critical role since they control the behaviour of the displacement of fluids in certain periods. In the case of sealing efficiency, as we mentioned previously, the capillary forces are fundamental to prevent the leakage and migration of the fluids in the reservoir (see 2.1).

4. Case studies

The samples used in the experiments performed in this work belongs to the Scioto sandstone (U.S.A.). This rock is part of the Mississippian formation, and it is commonly used to perform research in subsurface porous media. As seen in Figure 54, four core samples named SC1, SC2, SC3 and SC4 were used for this work.

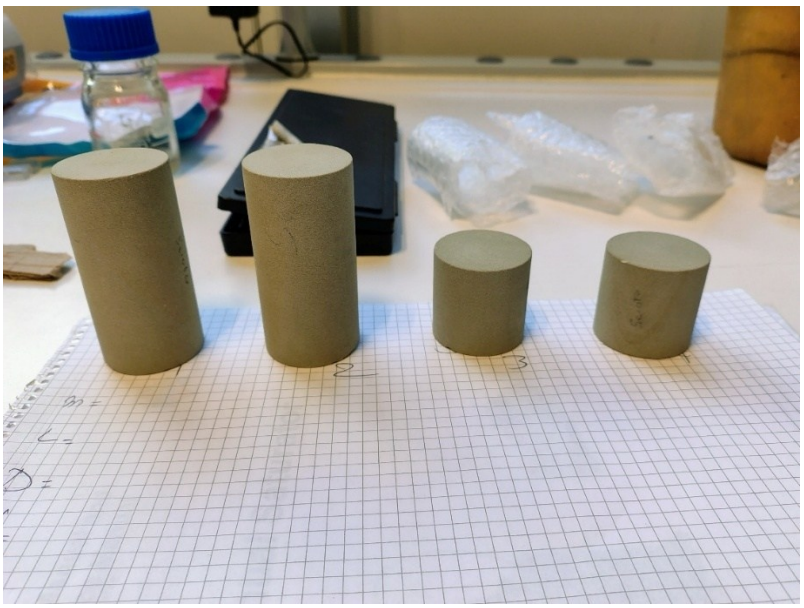

Figure 54: Core samples from Scioto Sandstone used. From left to right: SC1, SC2, SC3 and SC4.

The following table shows the basic characteristics of the samples:

Core Sample	Mass	Length	Diameter
SC1	190.191 g	7.65 cm	3.82 cm
SC2	190.73 g	7.64 cm	3.82 cm
SC3	96.115 g	3.85 cm	3.82 cm
SC4	96.134 g	3.85 cm	3.82 cm

Table 9: Characteristics of the core samples used.

Al-Kharra'a et al. [42] gave a detailed description of the mineralogical composition of the formation showing that the sandstone is mainly composed by quartz (almost 90 wt.%). The values are summarized in the following table:

Mineral	Wt.%
Quartz	89.2
Anhydrite	3
Illite	2.2
Plagioclase	2.1
Kaolinite	1
Chlorite	0.9
Orthoclase	0.7
Hematite	0.5
Siderite	0.2
Halite	0.2

Table 10: Mineralogical Composition of Scioto sandstone. Taken from [42].

During this work, some routine core analyses (RCA) were performed in these samples for a better characterization (e.g. porosity test and absolute permeability to water). The values obtained in those tests supported the results obtained later in the step-by-step experiments and gave a comprehensive characterization of the phenomenon.

4.1. Laboratory experiments and results

Porosity determination

The equipment used to measure the porosity of the samples was the PoroPerm from Vinci Technologies (Figure 55).

Figure 55: PoroPerm machine

The porosity measure done by this machine is the gas expansion test using nitrogen. This method is based in the ideal gas law:

$$PV = nRT$$ *Equation 18*

Where:
P: $Pressure$
V: $Volume$
n: $number\ of\ moles$
R: $Constant\ of\ gases$
T: $Absolute\ temperature$

The steps are:

- The rock is introduced and sealed in a container of known volume (V_1) at pressure P_1. This container is connected by a valve to another container of volume V_2 and pressure P_2 that contains nitrogen.
- The valve is opened, both containers are connected, and the gas occupies all the system.
- According to the ideal law of gases, since all the system is at the same temperature T and the amount of gas remains constant, the pore volume connected can be calculated using the following equation:

  $$P_2V_2 = P_3\left(V_1 + V_2 - V_{cs} + V_{p_{connected}}\right)$$ *Equation 19*

  Where:
  P_2: $Pressure\ of\ container\ 2\ at\ initial\ conditions$
  V_2: $Volume\ of\ container\ 2$
  P_3: $Pressure\ of\ the\ system\ (both\ containers)\ at\ equilibrated\ conditions$
  V_1: $Volume\ of\ container\ 1$
  V_{cs}: $Volume\ of\ core\ sample$
  $V_{p_{connected}}$: $Volume\ of\ connected\ pore\ volume\ in\ the\ core\ sample$

- Knowing the pore volume connected, the porosity can be calculated using:

  $$\emptyset_e = \frac{V_{p_{connected}}}{V}$$ *Equation 20*

  Where:
  $\emptyset_e$: $Effective\ porosity$
  $V_{p_{connected}}$: $Connected\ pore\ volume$

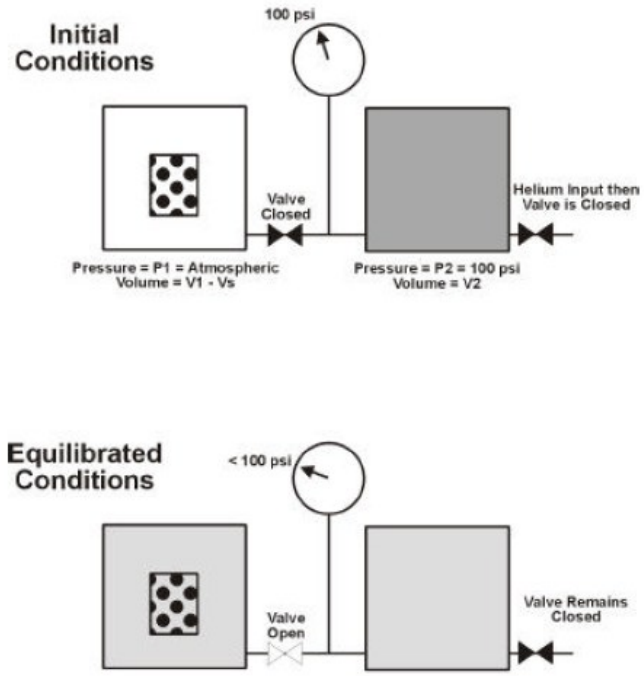

Figure 56: Diagram of a porosimeter [18]

The results obtained are presented in the following table:

Core Sample	Porosity	Pore Volume
SC1	18.86 %	16.53 cm^3
SC2	18.79 %	16.45 cm^3
SC3	18.75 %	8.27 cm^3
SC4	18.67 %	8.24 cm^3

Table 11: Porosities and pore volume of the samples

Permeability determination

The machine used was the Capillary Threshold Pressure Apparatus of Vinci Technologies. The test performed by this machine was the steady state method using tap water.

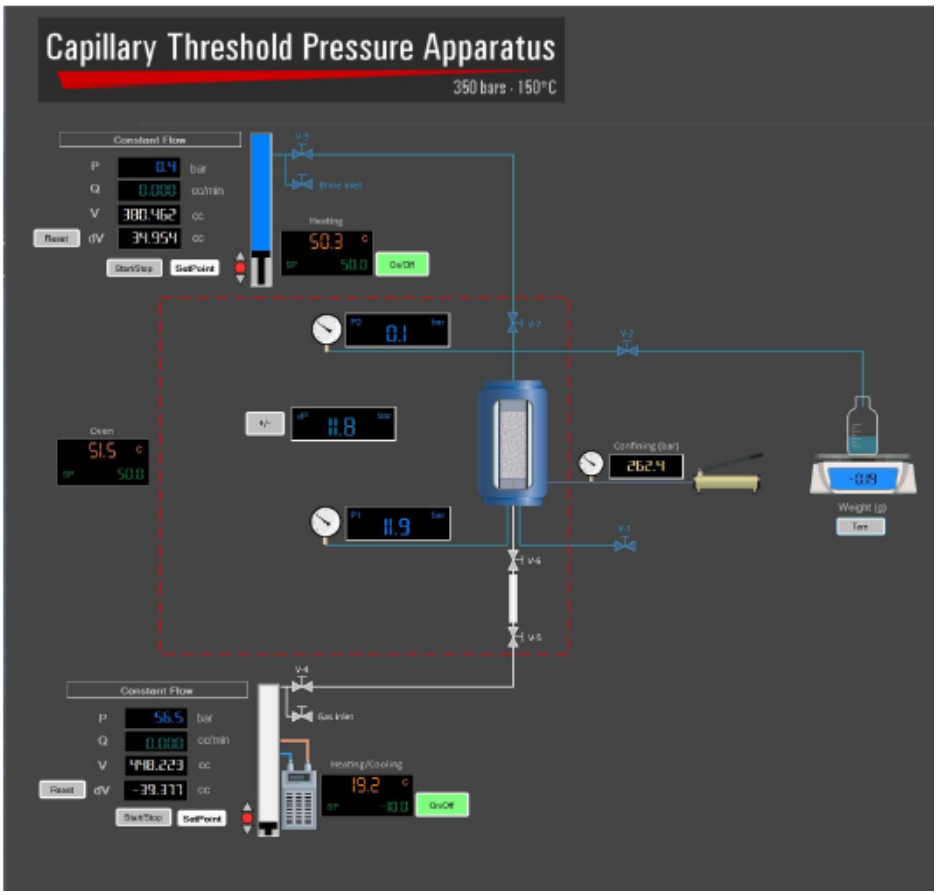

Figure 57: Scheme of the machine taken from the operational manual of Vinci Technologies.

The test consists in placing the core sample in the core holder and flowing water at different rates for enough time to obtain a stable flow. The pressure is measured in both extremes of the core sample (i.e. inlet and outlet) and the flow rate is recorded. The tests were done only in SC2 and SC3. SC1 was found to be broken and was therefore excluded from all analyses, while the permeability to water could not be measured in SC4 due to a malfunction of the equipment. The results obtained are shown in the following table:

Core Sample	**Rate**	**Pressure difference**	**Permeability**
SC3	2 cm^3/min	35.5 bar	0.315 mD
	1 cm^3/min	17.8 bar	0.318 mD
	0.25 cm^3/min	5.2 bar	0.273 mD
	0.5 cm^3/min	10 bar	0.284 mD
	Average		**0.298 mD**
SC2	2 cm^3/min	22.1 bar	1.02 mD
	$4cm^3/min$	42.7 bar	1.05 mD
	Average		**1.04 mD**

Table 12: Permeability to water test results

Breakthrough pressure determination

Four tests were performed to obtain the breakthrough pressure of the core samples. The method followed was the standard test (see 2.1.2.2) with five steps of 15 minutes each one in average. All of them under 50 bars of confining pressure. Two of the experiments in a sample of 7.64 cm length (SC2) and two in samples of 3.85 cm length (SC3 and SC4) to evaluate the impact of the variation of the dimensions in the breakthrough pressure. The project also investigates the potential effects of different temperature conditions on breakthrough pressure; hence, two experiments were performed in the same core sample under the same confining pressure and only variating the temperature. The two values of temperature used for the comparative experiment were 25°C and 50°C considering the operations range (up to 150°C), the information available on the literature about the influence of the temperature in the Nitrogen – water system (Figure 51) and the limitations of time to do the experiments.

The machine used was the Capillary Threshold Pressure Apparatus of Vinci Technologies (Figure 58).

Figure 58: Capillary Threshold Pressure machine

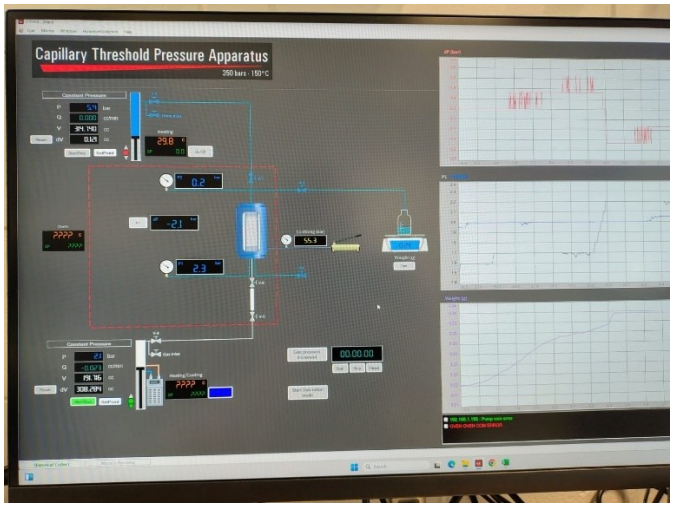

Figure 59: Software to control the apparatus and monitor the test.

The following tables show us the procedure of the tests, the conditions of each one and the results obtained:

Core Sample	Backpressure	Confining Pressure	Temperature	Step Number	Pressure difference	Time	Result
SC2	No	50 bars	25 °C	1	1.1 bar	15 min	--
				2	1.5 bars	15 min	Pbt detected
				3	2 bars	15 min	--
				4	2.5 bars	15 min	--
				5	3 bars	15 min	--

Table 13: Standard test steps performed in SC2 at 25°C

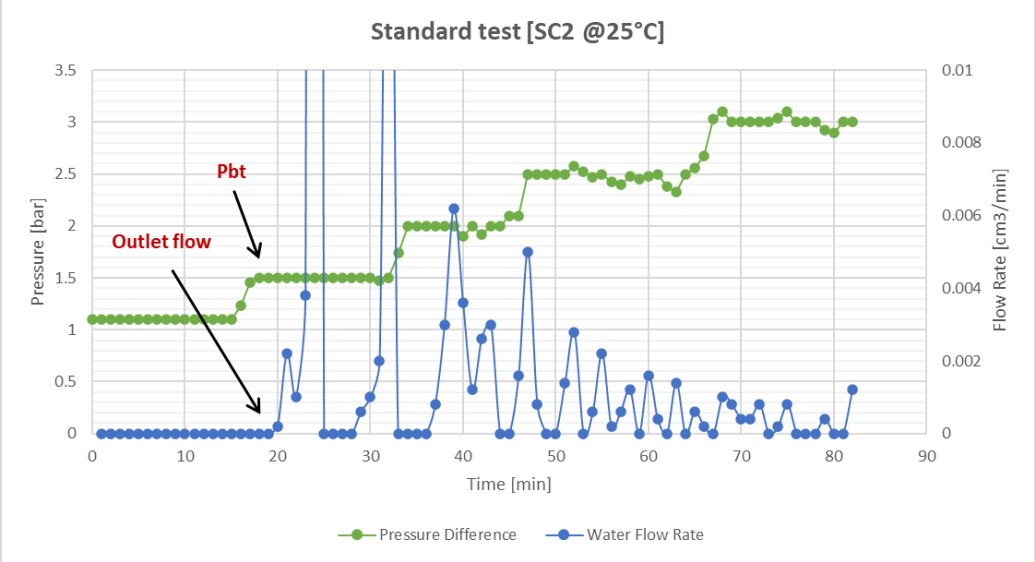

Figure 60: Standard test performed in SC2 at 25°C

Core Sample	Backpressure	Confining Pressure	Temperature	Step Number	Pressure difference	Time	Result
SC2	No	50 bars	50 °C	1	1.1 bar	15 min	--
				2	1.5 bars	15 min	Pbt detected
				3	2 bars	15 min	--
				4	2.5 bars	15 min	--
				5	3 bars	15 min	--

Table 14: Standard test steps performed in SC2 at 50°C

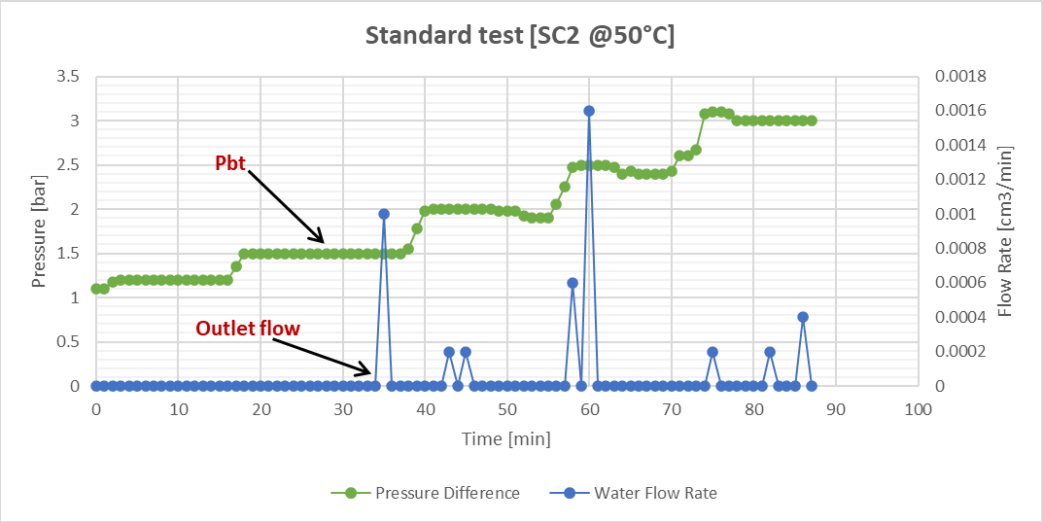

Figure 61: Standard test performed in SC2 at 50°C

Core Sample	Backpressure	Confining Pressure	Temperature	Step Number	Pressure difference	Time	Result
SC3	No	50 bars	25 °C	1	1.1 bar	12 min	--
				2	1.5 bars	12 min	--
				3	2 bars	15 min	--
				4	2.5 bars	15 min	--
				5	3 bars	15 min	Pbt detected

Table 15: Standard test steps performed in SC3 at 25°C

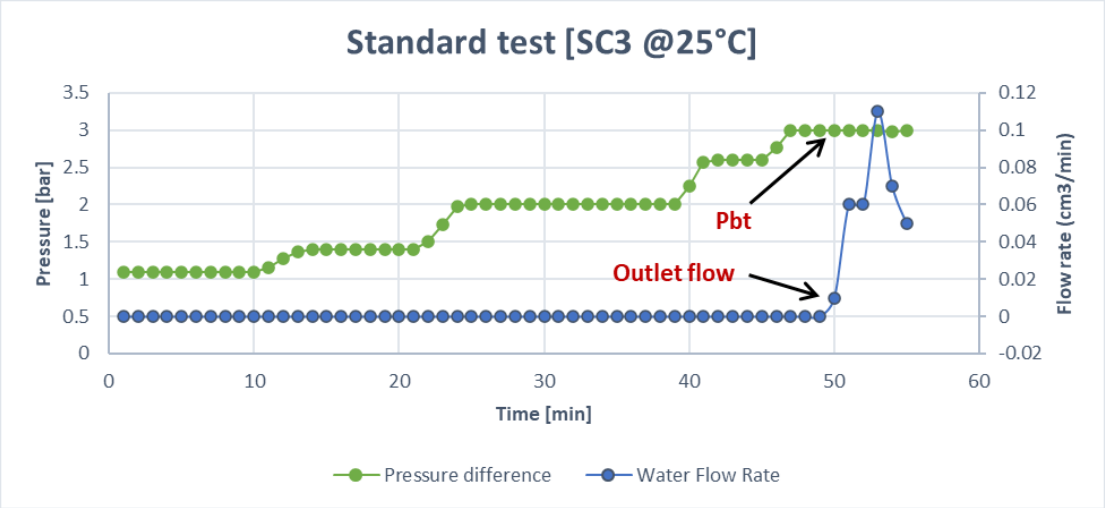

Figure 62: Standard test performed in SC3 at 25°C

Core Sample	Backpressure	Confining Pressure	Temperature	Step Number	Pressure difference	Time	Result
SC4	No	50 bars	25 °C	1	1.1 bar	15 min	--
				2	1.5 bars	15 min	--
				3	2 bars	15 min	--
				4	2.5 bars	15 min	--
				5	3 bars	15 min	Pbt detected

Table 16: Standard test steps performed in SC4 at 25°C

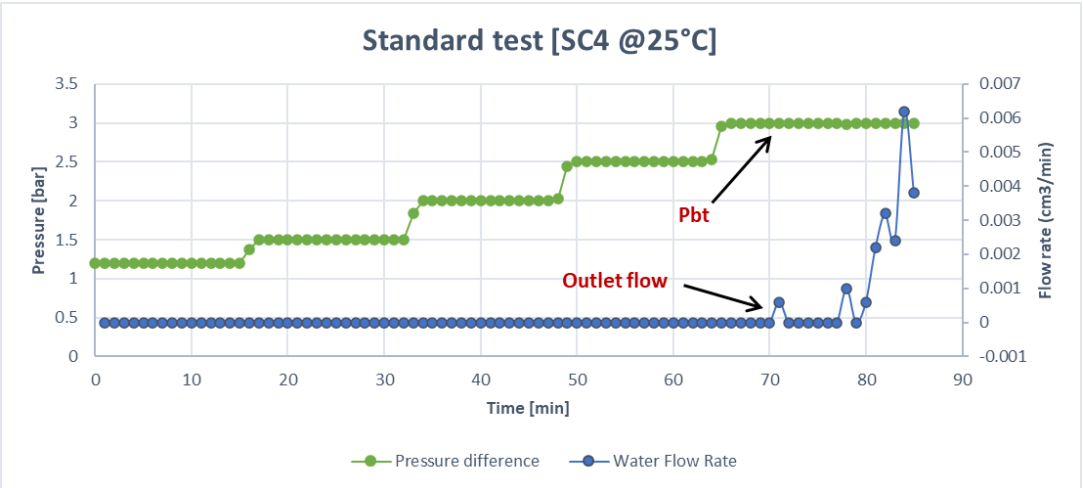

Figure 63: Standard test performed in SC4 at 25°C

The results of the tests are summarized in the following table:

Core Sample	Length	Porosity	Permeability	Backpressure	Confining Pressure	Temperature	Breakthrough pressure
SC1	7.65 cm	18.86%	N/D	--	--	--	N/D
SC2	7.64 cm	18.79 %	1.04 mD	No	50 bars	25 °C	1.5 bars
				No	50 bars	50 °C	1.5 bars
SC3	3.85 cm	18.75 %	0.298 mD	No	50 bars	25 °C	3 bars
SC4	3.85 cm	18.67 %	N/D	No	50 bars	25 °C	3 bars

Table 17: Summary of results of the tests

As shown in Table 17, there is not an appreciable influence of the temperature in the conditions of the experiment. Regarding this point, one should consider the relatively small difference between them following the limitations of the test and equipment. When it comes to the length and the permeability of the core sample there is an influence of both on the breakthrough pressure. However, from the experiments, it is not clear if both have the same influence on the results or if one overcomes the other.

4.2. Comparison between laboratory results and simulated values

The following images show us the comparison between the most representative laboratory results of water permeability and standard test and the simulated values.

1) Water permeability of core samples SC2 and SC3

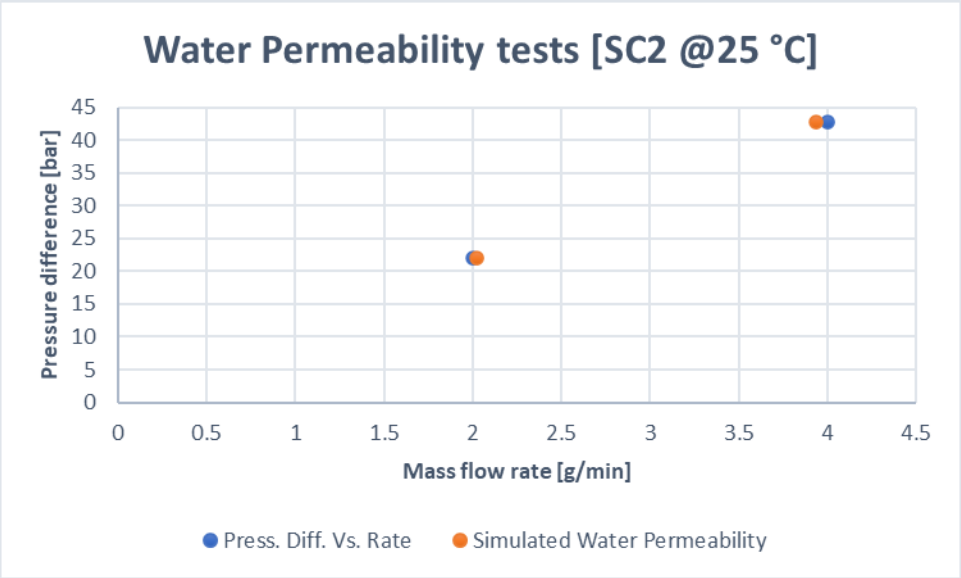

Figure 64: Comparison between real data and simulated values of the permeability test of SC2

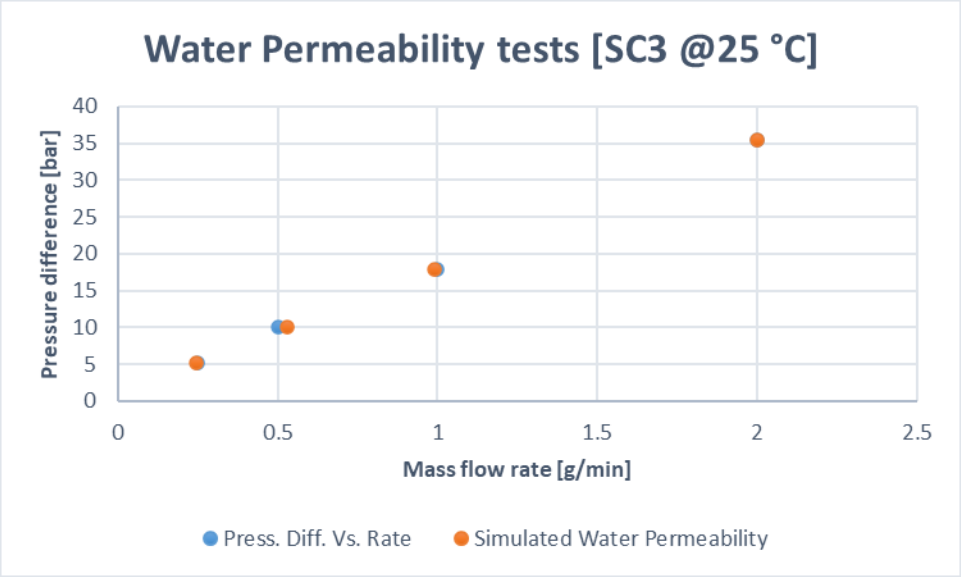

Figure 65: Comparison between real data and simulated values of the permeability test of SC3

Figure 64 and Figure 65 show an exact match between the measured values of absolute permeability and the simulations in the tests done in SC2 and SC3.

2) Standard test (step-by-step) on core samples SC2 and SC3 at 25°C

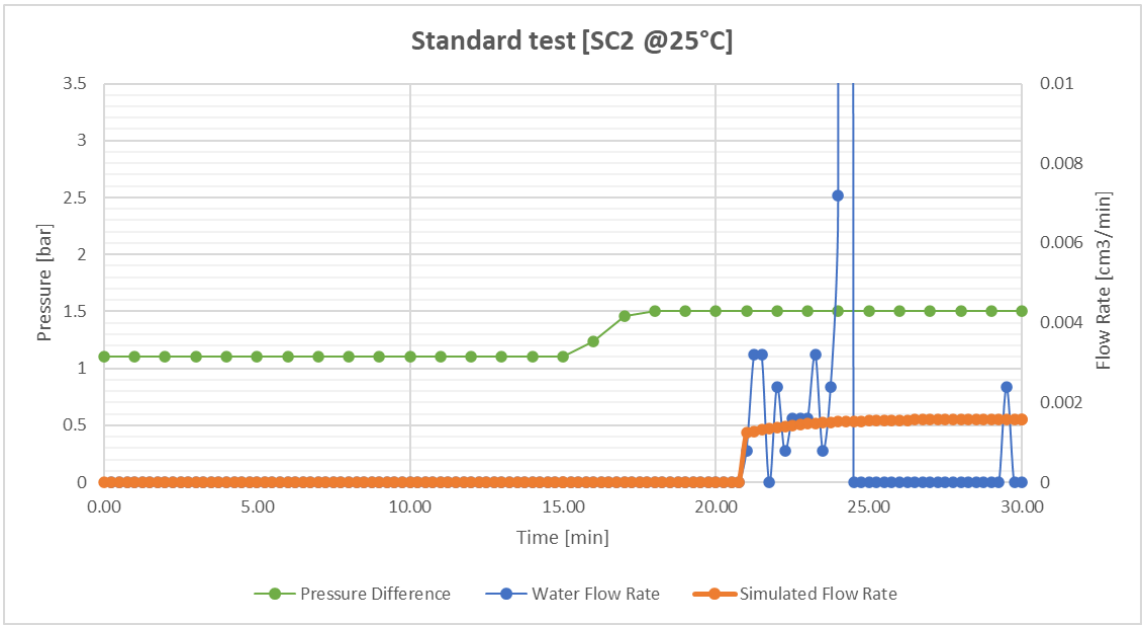

Figure 66: Comparison between real and simulated data up to the breakthrough of SC2 at 25°C

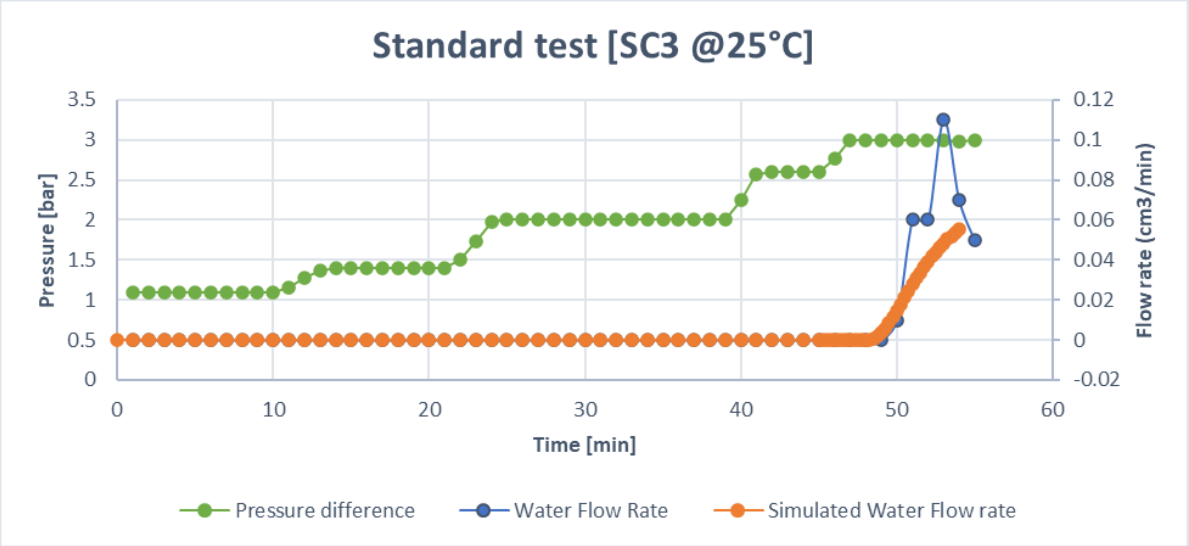

Figure 67: Comparison between real data and simulated values of the Standard test of SC3 at 25°C

Figure 66 and Figure 67 illustrate the good behaviour of the models simulating the standard tests performed in SC2 and SC3 at 25°C. In both cases, the model shows no outlet flow up to the breakthrough and the rate of flow after the breakthrough, in both cases is, on average, similar.

5. Conclusions

This project successfully characterizes the core samples of the Scioto formation through routine core analysis (i.e. porosity and absolute permeability) and compares the behaviour of the breakthrough pressure under different conditions such as length of the core samples, temperature and permeability. No significant variation in breakthrough pressure was observed under the evaluated temperature range (25°C to 50°C) in the same core sample. However, a decrease in breakthrough pressure was detected when comparing core samples with different lengths and permeabilities. Considering the theoretical influence of both factors, it is hypothesized that the effect of higher permeability compensated the influence of reduced core length.

Even though the limitations of the data used from the literature and the simplifications done, the model developed was able to successfully reproduced the experiments pursued in the laboratory being a powerful tool not only to obtain the capillary threshold pressure values as a first approximation or in case laboratory experiments are not possible to be run, but also to optimize the process of experimentation in tighter rocks such as shales in which the experiments may take weeks or months.

The numerical model can be used as a tool to have an idea of the values that we may obtain in case the thermodynamic conditions change but more laboratory experiments are recommended to determine the breakthrough pressure data varying pressure and temperature conditions.

Further work is recommended to determine which property-core sample length or permeability- has the greatest influence in the variation of the breakthrough pressure observed in this work. Other properties variation such as confining pressure, a wider temperature range and the use of tighter rocks is proposed to obtain more conclusive results. Finally, utilizing different gases such as methane, carbon dioxide, or hydrogen could offer a more comprehensive understanding of the breakthrough pressure.

6. References

[1] U. Nations, “Paris Agreement,” 2015. [Online]. Available: https://unfccc.int/files/essential_background/convention/application/pdf/english_paris_agreement.pdf.

[2] International Energy Agency, “World Energy Outlook,” International Energy Agency, Paris, 2023.

[3] BP, “BP Energy Outlook,” BP, 2024.

[4] TNO and EBN, “Sursurface Energy Storage is essential for the future energy system,” TNO and EBN, 2021.

[5] International Energy Agency, 2024. [Online]. Available: https://www.iea.org/energy-system/carbon-capture-utilisation-and-storage.

[6] Cedigaz, “Cedigaz,” 2022. [Online]. Available: https://www.cedigaz.org/underground-gas-storage-in-the-world-2023-status/.

[7] C. e. al., “The 2013 September–October seismic sequence offshore Spain: a case of seismicity triggered by gas injection?,” *Geophysical Journal International,* vol. 198, pp. 941 - 953, 2014.

[8] W. G. a. C. Frohlich, “Gas injection may have triggered earthquakes in the Cogdell oil field, Texas,” *PNAS,* vol. 110, no. 47, pp. 18786-18791, 2013.

[9] R. Weijermars, “Surface subsidence and uplift resulting from well interventions modeled with coupled analytical solutions: Application to Groningen gas extraction (Netherlands) and CO2-EOR in the Kelly-Snyder oil field (West Texas),” *Geoenergy Science and Engineering,* vol. 228, 2023.

[10] 2. Ringrose et al., “The In Salah CO2 Storage Project: Lessons Learned and Knowledge Transfer,” *Energy Procedia,* vol. 37, pp. 6226-6236, 2013.

[11] J. Kaldi, R. Daniel, E. Tenthorey, K. Michael, U. Schacht, A. Nicol, J. Underschultz and G. Backe, “Containment of CO2 in CCS: Role of Caprocks and Faults,” *Energy Procedia,* vol. 37, pp. 5403-5410, 2013.

[12] N. V. e. al., “HYDROCARBON COLUMNS OF OIL AND GAS FIELDS IN THE SOUTH SUMATRA BASIN,” *Berita Sedimentologi,* vol. 46, pp. 51 - 60, 2020.

[13] Earth Science Australia, “Earth Science Australia,” [Online]. Available: https://earthsci.org/mineral/rockmin/sed/sed.html. [Accessed October 2024].

[14] Virtual Geology, “Virtual-Geology Info,” [Online]. Available: https://www.virtual-geology.info/sediments-and-strata/sst-comp.html. [Accessed October 2024].

[15] S. B. Jr., Principles of Sedimentology and Stratigraphy, New Jersey: Pearson Prentice Hall, 2006.

[16] K. Bjørlykke, Petroleum Geoscience: From Sedimentary Environments to Rock Physics, Oslo: Springer, 2010.

[17] S. J. Boggs, Petrology of Sedimentary Rocks, New York: Cambridge University Press, 2009.

[18] P. W. J. Glover, Formation Evaluation MSc Course Notes, Aberdeen, 2001.

[19] D. Tiab and E. C. Donaldson, Petrophysics, Oxford: Gulf Professional Publishing, 2004.

[20] B. P. Tissot and D. H. Welte, Petroleum Formation and Occurence, Berlin: Springer-Verlag, 1984.

[21] Y. Shu, M. Wilkinson and N. Heinemann, "Using hydrocarbon fields of the UK North Sea as analogues for effective pore throat radii prediction in mudstone caprocks," *Energy Procedia,* vol. 114, p. 5329 – 5336, 2017.

[22] T. Ahmed, Reservoir Engineering Handbook, Boston: Elsevier, 2010.

[23] S. S. a. B. M. K. A. Hildenbrand, "Gas breakthrough experiments on fine-grained sedimentary rocks," *Geofluids,* vol. 2, pp. 3 - 23, 2002.

[24] V. Rocca, "Sealing Efficiency of Cap Rock [Lecture notes]," Politecnico di Torino, Turin, 2024.

[25] I. H. B. M. L. H. a. M. O. M. Eric W. Lemmon, "Thermophysical Properties of Fluid Systems," in *NIST Chemistry WebBook, NIST Standard Reference Database Number 69*, Gaithersburg MD, P.J. Linstrom and W.G. Mallard, National Institute of Standards and Technology, 2024.

[26] H. Mehrjoo, M. Riazi, M. N. Amar and A. Hemmati-Sarapardeh, "Modeling interfacial tension of methane-brine systems at high pressure and high salinity conditions," *Journal of the Taiwan Institute of Chemical Engineers,* vol. 114, pp. 125-141, 2020.

[27] M. Hosseini and Y. Leonenko, "Prediction of hydrogen□ brine interfacial tension at subsurface conditions: Implications for hydrogen geo-storage," *International Journal of Hydrogen Energy,* vol. 58, pp. 485-494, 2024.

[28] M. Hosseini, J. Fahimpour, M. Ali and A. Keshavarz, "H2□ brine interfacial tension as a function of salinity, temperature, and pressure; implications for hydrogen geo-storage," *Journal of Petroleum Science and Engineering,* vol. 213, 2022.

[29] C. Chalbaud, M. Robin, J.-M. Lombard, F. Martin, P. Egermann and H. Bertin, "Interfacial tension measurements and wettability evaluation for geological CO2 storage," *Advances in Water Resources,* vol. 32, pp. 98-109, 2009.

[30] P. Chiquet, J.-L. Daridon, D. Broseta and S. Thibeau, "CO2/water interfacial tensions under pressure and temperature conditions of CO2 geological storage," *Energy Conversion and Management,* vol. 48, pp. 736-744, 2007.

[31] N. Tonnet, D. Broseta and G. Mouronval, "Evaluation of the Petrophysical Properties of a Carbonate-rich Caprock for CO2 Geological Storage Purposes," *J Pet Technol,* vol. 62, 2010.

[32] P. K. Bikkina, "Contact angle measurements of CO2–water–quartz/calcite systems in the perspective of carbon sequestration," *International Journal of Greenhouse Gas Control,* vol. 5, pp. 1259-1271, 2011.

[33] G. Deng, J. Zhou, S. Tian, X. Xian, L. Zhou, C. Zhang, S. Li and Y. Tan, "Pore structure changes and its stress-sensitive behavior in sandstone under cyclic stress: Implication for underground gas storage," *Gas Science and Engineering,* vol. 119, 2023.

[34] K. Kashefi, L. M. Pereira, A. Chapoy, R. Burgass and B. Tohidi, "Measurement and modelling of interfacial tension in methane/water and methane/brine systems at reservoir conditions," *Fluid Phase Equilibria,* vol. 409, pp. 301-311, 2016.

[35] S. Bachu, "CO2 storage in geological media: Role, means, status and barriers to deployment," *Progress in Energy and Combustion Science,* vol. 34, pp. 254 - 273, 2008.

[36] W. R. Purcell, "Capillary Pressures - Their Measurement Using Mercury and the Calculation of Permeability Therefrom," *Petroleum Transactions,* pp. 39-48, 1949.

[37] S. Schlomer and B. M. Krooss, "Experimental characterisation of hydrocarbon sealing efficiency of cap rocks," *Marine and Petroleum Geology,* vol. 14, pp. 565-580, 1997.

[38] A. Busch and A. Amann-Hildenbrand, "Predicting capillarity of mudrocks," *Marine and Petroleum Geology,* vol. 45, pp. 208-223, 2013.

[39] L. K. Thomas, D. L. Katz and M. R. Tek, "Threshold Pressure Phenomena in Porous Media," *SPE Journal,* vol. 8, pp. 174 - 184, 1968.

[40] S. Li, M. Dong, Z. Li, S. Huang, H. Qing and E. Nickel, "Gas breakthrough pressure for hydrocarbon reservoir seal rocks: implications for the security of long-term CO2 storage in the Weyburn field," *Geofluids,* vol. 5, pp. 326-334, 2005.

[41] P. Egermann, J. M. Lombard and P. Bretonnier, "A fast and accurate method to measure Threshold Capillary Pressure of Caprocks under representative conditions," in *International Symposium of the Society of Core Analysis*, Trondheim, 2006.

[42] H. S. e. a. Al-Kharra'a, "Impact of clay mineralogy on the petrophysical properties of tight sandstones," *Geoenergy Science and Engineering,* vol. 227, 2023.

[43] Y. Chow, G. Maitland and J. Trusler, "Interfacial tensions of the (CO2 + N-2 + H2O) system at temperatures of (298 to 448) K and pressures up to 40 MPa," *Journal of Chemical Thermodynamics,* vol. 93, pp. 392-403, 2015.

[44] F. D. Eljabbar Latief, Z. Irayani, U. Fauzi and G. Dougherty, "The effect of X-ray micro computed tomography image resolution on flow properties of porous rocks: MICRO COMPUTED TOMOGRAPHY IMAGE RESOLUTION," *Journal of Microscopy ·,* vol. 266, no. 1, pp. 69-88, 2017.

[45] C. K. Ho and S. W. Webb, Gas Transport in Porous Media, Dordrecht: Springer, 2006.

[46] L. J. Klinkenberg, "The permeability of porous media to liquids and gases," *API Drilling and Production Practice,* pp. 200-213, 1941.

[47] D. D. Do, Adsorption analysis: Equilibria and Kinetics, London: Imperial College Press, 1998.

[48] S. Peng, "Advanced understanding of gas flow and the Klinkenberg effect in nanoporous rocks," *Journal of Petroleum Science and Engineering,* vol. 206, 2021.

[49] Olav Halsen et al., "Snøhvit: The History of Injecting and Storing 1 Mt CO2 in the Fluvial Tubåen Fm," *Energy Procedia,* vol. 37, pp. 3565-3573, 2013.

[50] G. e. al., "Challenges to and proposals for underground gas storage (UGS) business in China," *Natural Gas Industry,* vol. 4, pp. 231 - 237, 2017.

[51] Intergovernmental Panel on Climate Change, “Carbon Dioxide Capture and Storage,” Cambridge University Press, New York, 2005.

[52] G. M. Knebel and G. Rodriguez-Eraso, “Habitat of some oil,” *AAPG Bulletin,* vol. 40, pp. 547 - 561, 1956.

[53] A. F. Ismail, K. Khulbe and T. Matsuura, Gas Separation Membranes: Polymeric and Inorganic, Springer, 2015.

[54] M. A. Ibrahim, M. R. Tek and D. L. Katz, “Threshold pressure in gas storage,” *Pipeline Research Committee,* 1970.

[55] T. T. Schowalter, “Mechanics of secondary hydrocarbon migration and entrapment,” *AAPG Bulletin,* vol. 63, pp. 723-760, 1979.

[56] R. Pusch, L. Ranhagen and K. Nilsson, “Gas migration through MX-80 Bentonite,” Swedish Geological, Lund, 1985.

[57] C. Galle and K. Tanai, “Evaluation of gras transport properties of backfill materials for waste disposal: H2 migration experiments in compacted Fo-Ca Clay,” *Clays and Clay Minerals,* vol. 46, no. 5, pp. 498-508, 1998.

[58] M. R. J. Wyllie and W. D. Rose, “Some theoretical considerations related to the quantitative evaluation of the physical characteristics of Reservoir Rock from Electrical Log data,” *Petroleum Transactions,* vol. 189, pp. 105-118, 1950.

[59] E. L. Cussier, Diffusion: Mass transfer in fluid systems, New York: Cambridge University Press, 2009.

[60] American Petroleum Institute, Recommended Practices for Core Analysis, Washington: API Publishing Services, 1998.

[61] R. L. Slobod, A. Chambers and W. L. J. Prehn, “Use of Centrifuge for determining connate water, residual oil and capillary pressure curves of small core samples,” *Petroleum Transactions, AIME,* vol. 192, pp. 127-134, 1951.

[62] Z. E. Heinemann, Fluid Flow in Porous Media, Leoben: PHDG, 2005.

[63] H. Fu, X. Jian, W. Zhang and F. Shang, “A comparative study of methods for determining carbonate content in marine and terrestrial sediments,” *Marine and Petroleum Geology,* vol. 116, 2020.

[64] A. Chadwick, R. Arts, C. Bernstone, F. May, S. Thibeau and P. Zweigel, Best Practice for the Storage of CO2 in Saline Aquifers, Nottingham: British Geological Survey, 2008.

[65] J. W. Fentaw, H. Emadi, A. Hussain, D. Maury Fernandez and S. R. Thiyagarajan, “Geochemistry in Geological CO2 Sequestration: A Comprehensive Review,” *Energies,* 2024.

[66] P. Giesting, S. Guggenheim, A. F. Koster van Groos and A. Busch, “Interaction of carbon dioxide with Na-exchanged montmorillonite at pressures to 640 bars: Implications for CO2 sequestration,” *International Journal of Greenhouse Gas Control,* pp. 73-81, 2012.

[67] L. Hou, Z. Yu, X. Luo and S. Wu, “Self-sealing of caprocks during CO2 geological sequestration,” *Energy,* vol. 252, 2022.

[68] T. J. Katsube, B. S. Mudford and M. E. Best, “Petrophysics characteristics of shales from the Scotian Shelf,” *Geophysics,* vol. 56, pp. 1681-1689, 1991.

[69] A. Hildenbrand, S. Schlomer, B. M. Krooss and R. Littke, “Gas breakthrough experiments on pelitic rocks: comparative study with N2, CO2 and CH4,” *Geofluids,* vol. 4, pp. 61-80, 2004.

[70] Y. Yang and A. C. Aplin, “A permeability–porosity relationship for mudstones,” *Marine and Petroleum Geology,* vol. 27, pp. 1692-1697, 2010.

[71] J. Schon, Basic Well Logging and Formation Evaluation, Bookboon.com, 2015.

[72] G. R. Coates, X. Lizhei and M. G. Prammer, “NMR Logging Principles and Applications,” *Haliburton Energy Services Publication,* 1999.

[73] Z. Chen, F. Zhou and S. S. Rahman, “Effect of cap rock thickness and permeability on geological storage of CO2: laboratory test and numerical simulation,” *ENERGY EXPLORATION & EXPLOITATION,* vol. 32, pp. 943-964, 2014.

[74] L. Yu and N. C. Wardlaw, “The Influence of Wettability and Critical Pore-Throat Size Ratio on Snap-off,” *Journal of Colloid and Interface Science,* vol. 109, pp. 461-472, 1986.